JGR Oceans

RESEARCH ARTICLE

10.1029/2023JC020211

Key Points:

- Circulation pathways and volume transport of Atlantic- and Arctic-origin waters in the northwestern Barents Sea are detailed
- At the Polar Front density differences between these waters create a geostrophic current that governs warm water flow into the Arctic domain
- Over recent decades Atlantic Water warmed and freshened, reducing its density difference with the Polar Water and inflow across the front

Correspondence to:

I. Fer,
ilker.fer@uib.no

Citation:

Kolås, E. H., Baumann, T. M., Skogseth, R., Koenig, Z., & Fer, I. (2024). Circulation and hydrography in the northwestern Barents Sea: Insights from recent observations and historical data (1950–2022). *Journal of Geophysical Research: Oceans*, *129*, e2023JC020211. https://doi.org/10.1029/2023JC020211

Received 10 JUL 2023
Accepted 24 JUL 2024

Author Contributions:

Conceptualization: Eivind H. Kolås, Ragnheid Skogseth, Ilker Fer
Data curation: Eivind H. Kolås, Till M. Baumann, Ragnheid Skogseth, Zoe Koenig, Ilker Fer
Formal analysis: Eivind H. Kolås, Ilker Fer
Funding acquisition: Ilker Fer
Investigation: Eivind H. Kolås, Till M. Baumann, Ilker Fer
Methodology: Eivind H. Kolås, Till M. Baumann, Ragnheid Skogseth, Zoe Koenig, Ilker Fer
Software: Eivind H. Kolås, Ilker Fer
Supervision: Ilker Fer
Validation: Eivind H. Kolås, Till M. Baumann, Ragnheid Skogseth, Ilker Fer
Visualization: Eivind H. Kolås
Writing – original draft: Eivind H. Kolås

Circulation and Hydrography in the Northwestern Barents Sea: Insights From Recent Observations and Historical Data (1950–2022)

Eivind H. Kolås[1], **Till M. Baumann**[1,2], **Ragnheid Skogseth**[3], **Zoe Koenig**[1,4,5], **and Ilker Fer**[1,3]

[1]Geophysical Institute, University of Bergen and Bjerknes Center for Climate Research, Bergen, Norway, [2]Now at Institute of Marine Research, Bergen, Norway, [3]University Centre at Svalbard, Longyearbyen, Norway, [4]Norwegian Polar Institute, Tromsø, Norway, [5]Now at UiT - the Arctic University of Norway, Tromsø, Norway

Abstract The Barents Sea is one of the main pathways for warm and saline Atlantic Water (AW) entering the Arctic Ocean. It is an important region where water mass transformation and dense-water production contribute to the Atlantic meridional overturning circulation. Here, we present data from three cruises and nine glider missions conducted between 2019 and 2022 in the northwestern Barents Sea, and compare them with historical data collected between 1950 and 2009. We present circulation pathways, hydrography and volume transports of Atlantic- and Arctic-origin waters. Our observations show that 0.9 ± 0.1 Sv ($1\ \text{Sv} = 10^6\ \text{m}^3\ \text{s}^{-1}$) of Atlantic-origin water reaches the Polar Front (PF) region before splitting into several branches and eventually subducting beneath Polar Water (PW). The amount of Atlantic-origin water stored in the Olga Basin north of the PF is controlled by the density difference between AW and PW, and reached a maximum in the 90s when PW was particularly fresh. In the recent period from 2019 to 2022, the inflow of AW into the Barents Sea freshened by up to 0.1 g kg^{-1} compared to previous decades. This led to a reduction in the production of dense water, an increased temperature gradient across the PF, and a reduced poleward transport of warm water.

Plain Language Summary Warm and salty water from the Atlantic Ocean flows through the Barents Sea on its path toward the Arctic Ocean. It undergoes cooling and freshening due to interactions with the surrounding water and the atmosphere, and eventually encounters much colder and fresher Polar Water, creating a distinct boundary known as the Polar Front. We conducted several research missions in the northwestern Barents Sea between 2019 and 2022 and compared the data to historical records collected between 1950 and 2009. The cooled Atlantic Water sinks beneath the Polar Water before continuing toward the Arctic Ocean. In recent decades, the temperature of the Atlantic Water inflow has increased. The warm Atlantic Water can be traced below the Polar Front, leading to an increase in the temperature of the deeper waters north of the front. However, the amount of Atlantic Water north of the front is regulated by the density difference between the Atlantic Water and Polar Water. In the recent period of 2019–2022, the Atlantic Water reaching the front has become less salty. As a result, there is a reduced flow of warm water moving northward beneath the Polar Water and a larger temperature difference across the Polar Front.

1. Introduction

The Barents Sea is a shallow shelf sea, averaging about 230 m in depth (Figure 1). This sea accounts for about 10% of the Arctic Ocean's surface area and is characterized by ice-free, warmer waters in the south meeting ice-covered, colder waters in the north (Årthun et al., 2012; Helland-Hansen & Nansen, 1909; Loeng, 1991; Oziel et al., 2016; Smedsrud et al., 2013). The warm water comes from an extension of the North Atlantic Drift, originating from the Atlantic (R. Ingvaldsen et al., 2002; Orvik & Niiler, 2002; Poulain et al., 1996; Schauer et al., 2002), and the cold water originates in the Arctic Ocean through processes of ice melting and freezing, atmospheric cooling, and interactions with Atlantic-origin water (Lind & Ingvaldsen, 2012; Lind et al., 2018; Timmermans & Marshall, 2020). The current state of knowledge of the physical, chemical, and biological systems in the Barents Sea is reviewed in Gerland et al. (2023). The marginal ice zone, which marks the transition into ice-covered waters, is a vital area for primary production (Reigstad et al., 2002). The Barents Sea supports abundant commercial fish stocks, making it a critical region in Arctic ecosystems (Hamre, 1994; Johannesen et al., 2012; Reigstad et al., 2002). In addition, the southern Barents Sea is now ice-free year-round (Årthun

Writing – review & editing: Eivind H. Kolås, Till M. Baumann, Ragnheid Skogseth, Zoe Koenig, Ilker Fer

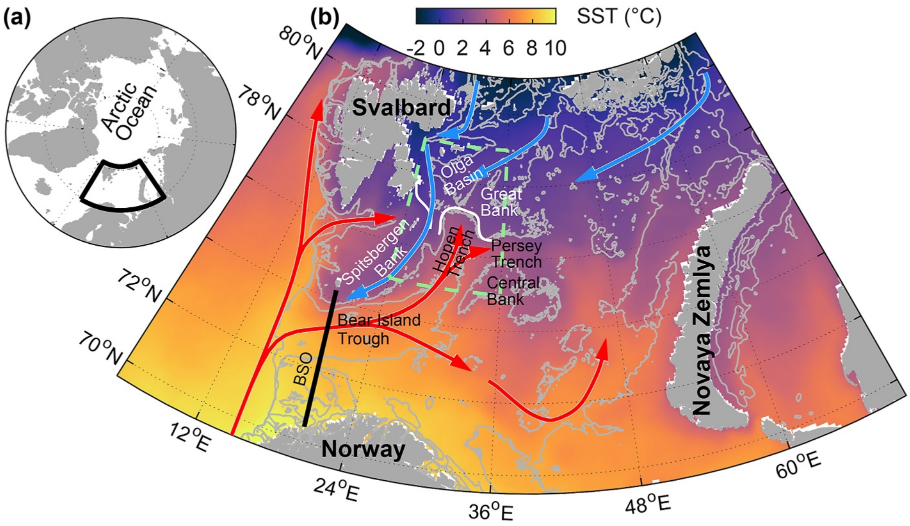

Figure 1. Overview map of the study region. (a) The Arctic Ocean where the black box encloses the Barents Sea shown in (b). (b) The Barents Sea. Red arrows outline the main Atlantic Water pathways. Blue arrows outline the pathways of Polar Water. Black line shows the Barents Sea Opening (BSO). Gray isobaths are drawn at 200, 350 and 500 m depth and are from IBCAOv4. Green dashed box encloses the study region. White line marks the location of the northwestern Barents Sea Polar Front. Sea surface temperature is the September-October mean between 2018 and 2022, and is from the product SEAICE_ARC_SEAICE_L4_NRT_OBSERVATIONS_011_008 at 0.05° resolution based upon observations from the Metop_A AVHRR instrument (Copernicus Marine Service, 2019).

et al., 2012; R. B. Ingvaldsen et al., 2021; Onarheim & Årthun, 2017), spurring increased interest in the exploitation of potential oil and gas resources in this shallow sea. To make sustainable decisions for the future in the Barents Sea, a thorough understanding of the ocean circulation and hydrography in the region is necessary.

The Norwegian Atlantic Slope Current transports Atlantic Water (AW) along the continental slope west of Norway (Fer et al., 2020; Orvik, 2022; Orvik & Niiler, 2002). North of Norway, at approximately 72°N, the slope current divides into two branches: one branch continues northward as part of the West Spitsbergen Current, while the other branch flows into the Barents Sea via the Barents Sea opening (BSO, Figure 1b). The average annual inflow of AW through the BSO is 2 Sv (1 Sv = 10^6 m^3 s^{-1}), when defined as water with temperatures above 3°C, reaching a maximum of 2.8 Sv in January and a minimum of 1.3 Sv in April (Skagseth et al., 2008; Smedsrud et al., 2010). This AW inflow is the primary source of oceanic heat for the Barents Sea. The observed transport estimates agree well with estimates based on regional ice–ocean model simulations, which indicate an average AW inflow through the BSO of 2.3 ± 0.4 Sv (Årthun et al., 2012). The total average inflow through the BSO, regardless of water mass, is about 3.2 Sv, of which 1.2 Sv is thought to recirculate within the Bear Island Trough, giving a net inflow through the BSO of 2 Sv (Loeng et al., 1997; Skagseth, 2008; Smedsrud et al., 2010).

The AW that flows into the Barents Sea is largely topographically steered, following the Bear Island Trough (Loeng, 1991). Once it reaches the Central Bank, the inflowing AW splits into two branches: one that continues eastward, south of the Central Bank, and another that moves northward along the Hopen Trench (Årthun et al., 2012; Loeng, 1991; Oziel et al., 2016). The branch south of the Central Bank occupies the southern half of the Barents Sea (Barton et al., 2018; Oziel et al., 2016). The partitioning of the AW transported in these two branches is unknown because of a lack of data to establish transport estimates. The Hopen Trench branch continues northward toward the Great Bank, where it again bifurcates: one branch flows eastward into the Persey Trench, and the other continues up the Hopen Trench (Loeng, 1991). The details of these branches, including their volume transport, pathways and modification as they reach the northern Barents Sea, are not well documented.

The northwestern Barents Sea is occupied by Polar Water (PW, water masses are defined in Section 3.1), which enters the Barents Sea from the north (Lien et al., 2017; Lind & Ingvaldsen, 2012; Loeng, 1991). The oceanographic front where PW meets AW is named the Barents Sea Polar Front (PF) (Loeng, 1991; Oziel et al., 2016; Våge et al., 2014). The PF is an important site for water mass transformation and has significant implications for local biogeochemistry and biology, as well as the overturning circulation and ventilation of the Arctic Ocean

(Årthun et al., 2011; Våge et al., 2014). The location of the PF has been remarkably stable in the western Barents Sea, following the 200–250 m isobath along the southern slope of the Spitsbergen Bank to the Great Bank (Gawarkiewicz & Plueddemann, 1995; Johannessen & Foster, 1978; Oziel et al., 2016). However, due to sparse data coverage, our current understanding of the circulation of AW south of the PF and the intricate patterns of circulation and mixing within the PF remains limited.

Studies on the southeastern slope of the Spitsbergen Bank have reported conflicting findings on the direction of the flow of AW. While some studies indicate that a warm-core jet of AW flows northeastward along the 300 m isobath (Li & McClimans, 1998; Loeng, 1991), others have observed a westward flow of AW on the southern slope of the Spitsbergen Bank, between the 260 and 400 m isobaths (Gawarkiewicz & Plueddemann, 1995; Parsons et al., 1996). The westward flow of AW is attributed to recirculating AW within the Bear Island Trough (Skagseth, 2008). Further observations suggest that northeast of the recirculating branch, AW flows clockwise around the Hopen Trench due to potential vorticity constraints in a basin with a shallower northern outflow depth than inflow (Barton et al., 2018). However, the circulation south of the PF in the Barents Sea is complex and influenced by various factors, including sea level, tidal flows, and winds, which change the dynamics of the front (Fer & Drinkwater, 2014; Våge et al., 2014). In addition, the position of the front on the southern slopes of the Spitsbergen Bank is affected by the climate of the Barents Sea, with the front shifting upslope in warmer periods with stronger winds from the south compared to colder periods (R. B. Ingvaldsen, 2005). These findings have important implications for the future PF as the Barents Sea transitions toward conditions where the inflowing AW is warmer and volume flux is larger (Skagseth et al., 2020; Smedsrud et al., 2022).

Time series of AW properties and transport through the BSO show that the temperature of the AW core increased by 1°C between 1965 and 2006, and the volume flux increased by 0.1 Sv per year between 1997 and 2006 (Skagseth et al., 2008). Note, however, that this strong trend estimate was partly caused by interannual variability. These observations are in agreement with more recent studies showing that the AW volume fraction in the Barents Sea has increased from about 10% in 1980 to about 30% in 2011 (Oziel et al., 2016). This so-called “Atlantification” has led to increased production and northward expansion of boreal species (R. B. Ingvaldsen et al., 2021), and has been strongly correlated with the retreat of the sea ice edge (Årthun et al., 2012). The sea ice area in the Barents Sea was reduced by 50% between 1998 and 2008, and the sea ice concentration has decreased by nearly 7% per decade from 1982 through 2020 (Årthun et al., 2012; Mohamed et al., 2022). However, the position of the PF in the western Barents Sea appears to be unaffected by the sea ice edge and has remained relatively stable, despite an observed increase in the sea surface temperature (SST) gradient associated with the PF (Barton et al., 2018).

The purpose of this paper is to provide a detailed account of the circulation and hydrography of AW in the northwestern Barents Sea, within the region enclosed in Figure 1b. Specifically, we concentrate on the area where the warm AW meets the cold PW, and thus maintains the PF. This area is of particular interest due to the limited knowledge of the route taken by the AW flowing northward toward the PF and the modification the AW undergoes along this route. We present recent observations and compare them to historical data collected in the same region.

2. Data

Detailed ocean hydrography and current profiles were collected from 2018 to 2021, focusing on the northwestern Barents Sea (Figure 1b). This comprehensive data set includes hydrography and current measurements from three scientific cruises and nine ocean glider missions, as well as shipboard acoustic Doppler current profiler (ADCP) data from five additional cruises spanning the same period. All of these data were obtained as part of the Nansen Legacy project. For convenience, we refer to this data set as the “recent data” or the “Nansen Legacy data.” The recent data primarily cover fall and winter, from August to February. In addition, we present historical data from the University Centre in Svalbard (UNIS) hydrographic database, consistently using the conductivity-temperature-depth (CTD) profiles collected between August and February. An illustration of data coverage and ship and glider tracks is provided in Figure 2. Detailed metadata for the cruises and glider missions where we collected hydrographic data are listed in Table 1.

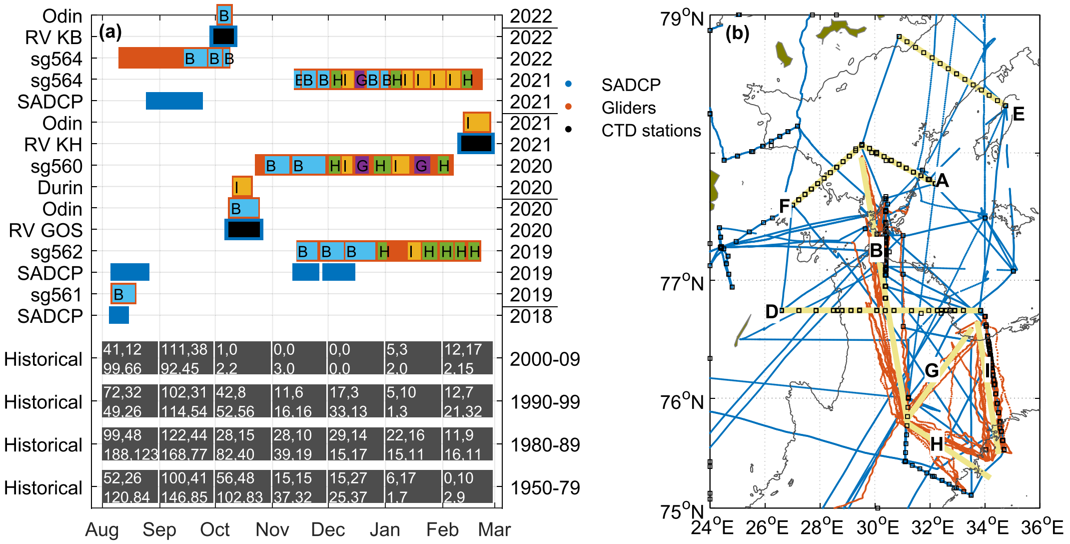

Figure 2. (a) Temporal and (b) spatial coverage of the data collected and presented in this study. The mission span of gliders is marked with orange fill in (a), and the mission tracks are shown in (b) using the same color. Sections are indicated by black uppercase letters and a color code in (a) to highlight the temporal coverage and repetitions of the sections. The positions of the sections are indicated by yellow lines in (b). Duration of cruises with shipboard ADCP (SADCP) data is indicated using blue fill in (a) and cruise tracks with the same color in (b). Specific cruises are identified with the vessel names RV KB: Kristine Bonnevie, RV KH: Kronprins Haakon, and RV GOS: G.O. Sars. The black fill for these cruises indicates shipboard CTD sampling, with stations marked with the same color in (b). The number of historical CTD profiles included in Sections B, H (upper two numbers), and D and I (lower two numbers) are listed in (a) for the individual months and decades. Gray line in (b) shows the 200 m isobath.

2.1. Hydrographic Measurements From the Nansen Legacy Cruises

The cruises were conducted on board the Research Vessel (RV) G.O. SARS between 6 and 27 October 2020 (Fer et al., 2021), RV Kronprins Haakon between 9 February and 1 March 2021 (Nilsen et al., 2021), and RV Kristine Bonnevie between 28 September and 13 October 2022 (Baumann et al., 2023). Conventional CTD profiles were collected during all cruises using the ship's Sea-Bird Scientific, SBE 911plus system. The salinity calculated from the ship CTD profiles was calibrated using water samples taken at all stations at the deepest profile depth. In total, 64, 89, and 62 profiles were collected using the ship's CTD system during the cruises, respectively. These CTD profiles, together with the current profiles (Section 2.2), from the three cruises are available from Fer, Skogseth, et al. (2023), Fer, Nilsen, et al. (2023), and Fer, Baumann, Koenig, et al. (2023), respectively. Pressure, temperature, and practical salinity data are accurate to ±0.5 dbar, $\pm 2 \times 10^{-3}$°C, and $\pm 3 \times 10^{-3}$, respectively. Ship CTD data were processed using the standard SBE Data Processing software.

In addition to the shipboard SBE CTD system, CTD profiles were collected using a Microstructure Sensor Profiler (MSS90L, Sea&Sun Technology, Germany; MSS hereafter). The MSS profiler is a loosely-tethered free-fall instrument equipped with turbulence sensors (not reported here) and CTD sensors. The profiles from the CTD sensors of the MSS profiler have been corrected against the ship CTD profiles during post-processing, by applying offsets where applicable. The largest salinity offset applied was 0.018 (Table 1). A total of 205, 172 and 266 profiles were collected using the MSS profiler during the three cruises, respectively, which can be obtained from Fer, Baumann, Elliot, and Kolås (2023), Fer, Baumann, Kalhagen, et al. (2023), and Fer, Baumann, Hana, et al. (2023).

Conservative Temperature, Θ, and Absolute Salinity, S_A, were calculated using the thermodynamic equation of seawater (IOC et al., 2010), and the Gibbs SeaWater Oceanographic Toolbox (McDougall & Barker, 2011).

2.2. Current Profiles From Cruises

Current profiles were obtained using ADCPs in two different configurations: ship-mounted ADCP (SADCP) for continuous measurements and ADCP systems integrated into the ship's CTD frames (lowered-ADCP, LADCP) for station-based measurements. The CTD frames on all vessels were equipped with a pair of 300 kHz Teledyne

Table 1
Metadata for the Cruises and Glider Missions Where We Collected Hydrographic Data

Platform	Start/end	Sections	Total CTD profiles	Offset applied to salinity/temperature
sg561	7 August 2019/ 19 August 2019	B	308	0.016/0.082°C
sg562	15 November 2019/ 1 March 2020	B, H, I	2,568	−0.005/−0.060°C
RV GOS	6 October 2020 27 October 2020	B, H, I, D, F, A, E	269	−0.018/–
Odin	8 October 2020/ 24 October 2020	Polar Front	800	0.014/0.054°C
Durin	10 October 2020/ 20 October 2020	I	678	–/–
sg560	22 October 2020/ 11 February 2021	B, H, I, G	2,534	0.017/−0.209°C
RV KH	9 February 2021 1 March 2021	B, I	261	−0.018/–
Odin	12 February 2021/ 25 February 2021	I	748	0.0045/0.05°C
sg564	12 November 2021/ 22 February 2022	B, H, I, G	3,426	0.015/0.02°C
sg564	9 August 2022/ 9 October 2022	B	2,492	0.015/0.02°C
RV KB	28 September 2022 13 October 2022	D, I, B F, A	328	–/–
Odin	2 October 2022/ 9 October 2022	Polar Front	402	–/–

Note. Sections refer to the section names listed in Figure 2b. The number of CTD profiles from the cruises is the sum of the profiles collected using the ship's CTD system and the profiles collected using the MSS profiler. Offsets of salinity and temperature are corrections against the ship's CTD measurements, and applied to the profiles collected by gliders and the MSS profiler.

RD Instruments (RDI) Workhorse Sentinels, with one mounted pointing downward and the other upward. The LADCPs were synchronized and configured to provide vertically averaged data in 8 m bins. Compasses were calibrated to reduce directional uncertainties to less than 5°. LADCP data were processed using the LDEO software version IX-13 of Visbeck (2002). The LADCP profiles were constrained using navigation data and the current profiles from the SADCPs.

All research vessels were equipped with Teledyne RDI Ocean Surveyor SADCPs. In this study, we use the current profiles collected by the 150 kHz SADCP from RV Kronprins Haakon and RV Kristine Bonnevie, and the 75 kHz SADCP from RV G. O. SARS. The SADCPs on Kronprins Haakon were flush-mounted in the hull for protection when moving through ice. The 150 kHz SADCPs collected profiles in 4 m bins using narrowband mode for optimal range, while the 75 kHz SADCP measured in 8 m bins. SADCP data were collected using the onboard VmDAS software or the University of Hawaii data acquisition software, depending on the vessel. Post-processing was done using the University of Hawaii CODAS software, to an uncertainty of 2–3 cm s^{-1} (Firing & Ranada, 1995).

In addition to the current measurements obtained during the specific cruises described in this study, we also incorporate SADCP data from five additional cruises conducted in the region during the fall and winter seasons (August to February) between 2018 and 2020. For more detailed information regarding the SADCP data obtained from these additional cruises, the reader is referred to Cannaby et al. (2022).

2.3. Ocean Glider Data

An ocean glider (glider hereafter) is a buoyancy-driven, remotely-piloted underwater vehicle. Five Kongsberg Seaglider missions and four Teledyne G3 Slocum glider missions were conducted in the Barents Sea in the period from 2019 to 2022. The glider data are available from Kolås et al. (2022) and Fer et al. (2024). Details about the individual missions are shown in Table 1. The main objective was to map the distribution and circulation of the AW in the region (Figure 1), and to collect detailed observations on the interaction between the AW and PW along the Polar Front between the Spitsbergen Bank and the Great Bank. The glider tracks are shown in Figure 2b, and the sections sampled by the individual gliders are listed in Table 1 as well as shown in Figure 2a. A total of 13,956 profiles were collected and analyzed. The typical horizontal distance between subsequent surfacing locations was 1 km. Both types of gliders were equipped with CTD sensors and operated between the surface and 0–20 m above the seafloor, sampling CTD on both descents and ascents. Specific processing details for each type of glider are described in the subsections below. For each dive, a depth-averaged current (DAC) was estimated based on the deviation between the actual surfacing location and the expected surfacing location from a hydrodynamic glider flight model. Absolute geostrophic currents were calculated from hydrography profiles and DAC, as described in Section 3.2. During post-processing, each profile from both types of gliders was despiked by flagging values exceeding twice the root mean square (rms) value of (x–xs), where x is the profile data and xs is a five-point median filter. Finally, for each mission, at each pressure level, outliers exceeding three standard deviations over all profiles of that mission at that pressure level were removed.

2.3.1. Seagliders

Each of the Seagliders was equipped with a Kistler piezoresistive pressure sensor, a SBE CT Sail and an Aanderaa dissolved oxygen sensor. The Seagliders operated with a vertical velocity close to 8 cm s^{-1}, and sampling rates normally aimed to sample conductivity and temperature every meter while oxygen was sampled every 5 m. The Seaglider data sets were processed using the University of East Anglia Seaglider toolbox, based on the methods described by Garau et al. (2011) and Frajka-Williams et al. (2011). Obvious outliers in the salinity and temperature profiles were manually flagged before applying a hydrodynamic flight regression (Frajka-Williams et al., 2011) to obtain improved estimates of flow past the CT Sail. The flow past the CT Sail is important for improved salinity and temperature calculations from the unpumped CT sensor. Using the improved salinity and temperature profiles, we applied the thermal lag correction of salinity data (Garau et al., 2011), before performing a detailed manual quality control of the salinity and temperature profiles. Processed S_A and Θ are accurate to 0.01 g kg^{-1} and 0.001°C, respectively, and DAC is accurate to 0.01 m s^{-1} (Seaglider Quality Control Manual, 2012, p. 9). Post-processing revealed noisy data with overturns, typically through the pycnocline and the apogee of the dive, but also randomly throughout profiles. The noisy data is likely a result of the CT sensor being unpumped: when the flow past the sensor changes due to a change in pitch or vertical velocity, the salinity estimates can be erroneous due to a misalignment of conductivity and temperature. Because of the uncertainty in the salinity estimates, we removed instabilities where the absolute difference between the density profile and the sorted-density profile was larger than 0.02 kg m^{-3}. The number of data points removed was less than 1% of the total data, and overall does not affect the averaged and objectively mapped fields used in our analysis. Finally, salinity and temperature offset corrections were applied after comparing the deep part of Seaglider dives to nearby CTD profiles collected from research vessels typically within 3 days and 5 km from the glider profile. Often only one ship CTD profile was available for comparison, yet, using one offset value to match the deep layer average salinity is justifiable for such short (several months) sampling durations where we expect insignificant instrumental drift. The offsets applied to the different missions are listed in Table 1.

The gliders in the Barents Sea were operated with an ice-avoidance algorithm in order to prevent losing the instrument in the ice. This algorithm uses acoustics to detect ice keels in addition to temperature measurements to identify freezing temperatures near the surface. If sea ice or near freezing-point temperatures were detected, the glider would initiate a dive without surfacing. On several occasions, northerly winds pushed sea ice over the gliders, preventing them from surfacing and obtaining a GPS fix. These events normally lasted for only a few dives, but on a few occasions the glider was under ice for longer than 24 hr, causing the glider to head to a predefined point away from the ice (so-called “escape mode”). The longest stretch without a GPS fix lasted for 34 dives or about 44 hr. In such situations without a GPS fix, DAC cannot be estimated. For each dive conducted without a GPS fix, longitude and latitude coordinates along the dive tracks were linearly interpolated between the two available GPS fixes, assuming the glider continued in a straight line. In the few cases when the glider turned south in the escape mode while under sea ice, the northernmost position was extrapolated based on the most recent horizontal velocity estimate, the compass heading, and the depth of the seabed. More details on the processing and glider deployments are given in Kolås et al. (2022).

2.3.2. Slocum Gliders

Two electric 1,000-m G3 Slocum gliders, “Odin” and “Durin,” were used during the October 2020 cruise, while Odin was also used during the February 2021 and October 2022 cruises (Table 1). Both gliders carried a pumped SBE CTD sensor (CTD41CP). The glider sampled at 0.25 Hz with a typical vertical velocity of 15 cm s^{-1}. The glider was configured to inflect 15 m above the seabed. Data were processed using the quality control procedures from the Balearic Islands Coastal Observing and Forecasting System (SOCIB) data processing toolbox (Troupin et al., 2015). Final profiles have a horizontal along-track spacing of about 0.5 km and a vertical spacing of 1 m. Odin additionally carried a turbulence package for measuring small-scale shear across the Polar Front. The turbulence data set is discussed in Kolås et al. (2024) and is not further described here.

Table 2
Water Mass Definitions Following Sundfjord et al. (2020), Using Conservative Temperature, Θ, Absolute Salinity, S_A, and Potential Density Anomaly, σ_0

Water mass	Θ (°C)	S_A (g kg^{-1})	σ_0 (kg m^{-3})
Atlantic Water (AW)	$\Theta \geq 2$	$S_A \geq 35.06$	
Polar Water (PW)	$\Theta < 0$		$\sigma_0 < 27.97$
Warm Polar Water (wPW)	$\Theta \geq 0$	$S_A < 35.06$	$\sigma_0 \geq 27.8$
Surface Water (SW)	$\Theta \geq 0$	$S_A < 35.06$	$\sigma_0 < 27.8$
Modified Atlantic Water (mAW)	$0 \leq \Theta < 2$	$S_A \geq 35.06$	
Intermediate Water (IW)	$-1.1 \leq \Theta < 0$		$\sigma_0 \geq 27.97$
Cold Barents Sea Dense Water	$\Theta < -1.1$		$\sigma_0 \geq 27.97$

Note. Our definition of the warm Polar Water (wPW), includes only waters with $\sigma_0 \geq 27.8$ in order to exclude surface waters from the wPW. Instead, we name the wPW with $\sigma_0 < 27.8$ Surface Water (SW).

2.4. Historical Data

Historical composite sections of Conservative Temperature and Absolute Salinity over the periods 1950–1979, 1980–1989, 1990–1999, and 2000–2009 were made from hydrographic profiles extracted from the UNIS hydrographic database (UNIS HD; Skogseth et al., 2019). This data set is a collection of temperature and salinity profiles from the area 0°–34°E and 75°–83°N. Duplicate data and outliers have been removed before the analysis. In this study we only considered CTD profiles collected between August and February, and a total of 3,916 profiles were included. Note that UNIS HD also consists of data extracted from other data publishers. For details on the main data contributors to UNIS HD, the reader is referred to Skogseth et al. (2019).

3. Methods

3.1. Water Masses

The water masses used in this study are listed in Table 2, and follow Sundfjord et al. (2020). These definitions are based on previous water mass definitions in literature such as in Lind et al. (2018), Loeng (1991), and Rudels et al. (2005). However, we have made a modification to the definition of warm Polar Water (wPW), by including only waters with potential density anomaly $\sigma_0 > 27.8$. The reason for this is that we only consider the wPW which is a mixture between AW and PW, excluding surface waters influenced to a greater extent by seasonal processes such as atmospheric heating and ice melting. In the following, Atlantic-origin waters refer to AW and AW that has been cooled and freshened en-route through interaction with the atmosphere, sea ice, and surrounding water masses. This definition includes both wPW and modified AW (mAW).

3.2. Objective Interpolation of Depth Average Currents

In this study, a total of 59,000 SADCP profiles, 198 LADCP profiles and 7,195 DAC estimates from glider dives have been used. We removed the barotropic tidal currents from the SADCP and LADCP profiles using the 2018 version of the Arctic Ocean Inverse Tidal Model on a 5 km grid (Arc5km2018) (Padman & Erofeeva, 2004). LADCP profiles were vertically averaged over the whole water column, whereas for the SADCP profiles, the upper 16 m were removed before averaging (16 m was the largest blanking distance used on the different SADCPs). Depth-averaged SADCP currents were subsequently bin-averaged in 10 km by 10 km horizontal bins.

A typical glider dive in the Barents Sea lasted for about an hour and covered about 1 km horizontal distance. To remove the barotropic tide from DAC, we interpolated the DAC time series to hourly data and used a 24 hr low pass filter. The detided DAC were then averaged over 6 hr bins. A final 10 km by 10 km bin-averaging was applied to combine the detided and averaged SADCP, LADCP and glider DAC before objective interpolation. We constrained the interpolated fields to be divergence-free, and used a horizontal correlation length scale of 50 km, obtained from a variogram analysis of the depth averaged currents after final bin-averaging. Variogram analysis calculates the variance in the difference between data points as a function of the distance between the data points. The correlation length scale is then set at the distance where the variance ceases to increase. More details on variogram analysis are given in the appendix of Kolås et al. (2020). We objectively interpolated onto a horizontal grid with 10 km resolution. Mapped currents for which the relative error exceeded 40% of the absolute current were removed. We also removed currents mapped at locations where the water depth was shallower than 50 m. The 50 m depth criterion was set as we have few measurements in the shallow regions where the tidal currents are relatively large.

3.3. Composite Sections

In order to remove fine-scale variability and to obtain fields representative of the average hydrography and geostrophic currents, we produce composite sections. The composite sections are along the predefined transects marked by yellow lines in Figure 2b, along which we have focused our measurements. The horizontal grid spacing along each section was set to 1 km. For every data point (all Θ and S_A profiles, and SADCP and glider DAC), an incrementally increasing search radius of 5, 10, 20 and 30 km was used to look for predefined grid points along the target section. When two or more grid points were within the search radius of a data point, the data point was moved along isobaths onto the section, thus assuming topographic steering. The bottom depth along the section, as well as for the data points, was determined using IBCAO-v4 bathymetry (Jakobsson et al., 2020). If by chance two or more locations on the predefined section (within the search radius of the data point) had the same bottom depth, the location nearest to the data point was chosen. Finally, Θ and S_A profiles along the section were bin-averaged over 5 km horizontal and 10 m vertical bins before objectively mapping onto a 1 km by 5 m grid (horizontal by vertical). Historical CTD profiles were averaged over 5 km horizontal and 20 m vertical bins before objectively mapping onto a 1 km by 5 m grid. To obtain absolute geostrophic velocities along the composite sections, we need reference depth-averaged velocities averaged and smoothed with consistent time and length scales. Depth-averaged SADCP velocities and glider DAC were bin-averaged over 5 km horizontal bins and linearly interpolated onto the 1 km resolution of the target section, and smoothed using a 15 km moving average.

When objectively mapping the composite sections, correlation lengths of 30 km and 50 m were used as horizontal and vertical scales, respectively, determined from the variogram analysis as described in Section 3.2. To remove unrealistic values caused by interpolation, temperatures below freezing were set to the freezing point, and values below the seabed were removed. In addition, mapped values for which the relative error (the absolute error divided by the data value) exceeded 5% were removed. The low threshold of 5% was used due to the high resolution of data points compared to the long correlation length. That is, we have binned observations for every 5 km along the section while using a 30 km correlation length scale, resulting in a small objective mapping error.

We produced relative geostrophic velocity fields referenced to the surface using the objectively mapped Θ and S_A sections from the cruises and gliders, and the historical section across the PF (Section B). To avoid spurious unstable layers arising from the combination of the independently mapped fields, we calculated potential density and reproduced the S_A fields using sorted (by stability) and smoothed potential density. Potential density was smoothed over 2 km horizontal and 10 m vertical distance (2 by 2 grid points). When analyzing data from recent years, where we have depth-averaged currents, absolute geostrophic velocity, u_g, was obtained by removing the depth-averaged from the relative geostrophic velocity field, and adding depth-averaged gridded observed SADCP and glider DAC.

As we estimate mean properties and volume transports from objectively mapped fields of Θ, S_A, and u_g, the uncertainty in our measurements has to be considered. While the measurement error of the individual instruments is small (high precision), the accuracy of the measurement can be small because of calibration error and other factors. The ship CTD measurements are the most accurate; the sensors are routinely calibrated and the salinity calculations are corrected against water sample analyses. Here we cross-calibrate the temperature and salinity profiles from gliders and MSS by applying a constant offset, if needed, after comparing against selected profiles from the ship's CTD system. While the ship CTD profiles and the MSS profiles we compare are conducted at nearly the same location and often within the same hour, the ship CTD profiles and the glider profiles may have some distance between them. The ship profiles and glider profiles we compare are generally separated by less than 5 km and 3 days. However, the region is highly dynamical (especially the front region) and comparison may be subject to inaccuracies. To reduce the effects of temporal and spatial variability, we use the deeper part of the profiles, particularly within trenches, to obtain the offset values. We expect insignificant instrumental drift in glider measurements over such short sampling durations (several months) and argue that the uncertainty in our Θ and S_A measurements is of a similar magnitude to the offsets we typically apply. That is 0.02 g kg^{-1} and 0.1°C for S_A and Θ, respectively, rounded to the first significant digit (Table 1).

Volume transport estimates for individual water masses are calculated from the u_g fields. These estimates are most sensitive to the water mass boundaries and the 2–3 cm s^{-1} SADCP uncertainty. Here we estimate the error by applying an upper and lower bound on the water mass boundaries corresponding to the S_A and Θ uncertainty. Then we add one thousand Gaussian distributed random error matrices where the error ranges from −3 to 3 cm s^{-1} corresponding to the SADCP uncertainty. Errors are the root-mean-square of the difference between calculations from the original gridded field and each of the upper and lower boundary. The resulting volume transport error is always less than 0.1 Sv, and typically around 0.05 Sv.

3.4. Objectively Interpolated Horizontal Layers

Objectively mapped horizontal fields of Θ and S_A for different depth layers (50–100 m, 100 m to bottom) and different time periods were produced using the recent and historical CTD profiles. Individual profiles were vertically averaged over the desired layer depth, before bin-averaging over 10 km by 10 km horizontal bins. To ensure that the vertically averaged values were representative of the layer, we set thresholds on the minimum number of data points averaged, and on the deviation of the average depth of data points from the middle depth of the layer. For the 50–100 m layer, a minimum of 5 data points whose mean depth was within 15 m of the middle depth of the layer were required. Horizontal correlation length scales were set to 60 km and the final gridded product had a 2 km resolution.

3.5. Barents Sea Polar Front Position

The position of the PF is determined following the method described by Oziel et al. (2016). Oziel et al. (2016) calculated two different fronts, a northern and a southern front based on temperature and salinity, respectively. In our study, we focus only on the position of the northern front obtained from the temperature field. To achieve this, we create a horizontally mapped field by combining all available temperature data for the 50–100 m layer, including both historical and recent data, using the method described in Section 3.4. Subsequently, we calculate the magnitude of temperature gradients across this field. We then construct a histogram with 0.05°C bins of the Θ values where the temperature gradient exceeds 0.06°C km^{-1}. The PF is then defined as the isotherm corresponding to the modal value of the histogram, here equal to the 0.1°C isotherm, with a standard deviation of 0.4°C. While the modal value is somewhat sensitive to the temperature gradient threshold, the position of the front along Section B varies less than 15 km, within ±0.4°C (one standard deviation) of the modal value.

4. Results

The AW inflow into the Barents Sea is a topographically steered current, following the (south-) eastern boundary of the Bear Island Trough. Here we describe the evolution of the AW from the northeasternmost part of the Bear Island Trough where the AW splits into two paths; one toward the Hopen Trench and one toward the Persey Trench (Figure 1b). Subsequently, we describe the continuation of Atlantic-origin waters from the Hopen Trench across the PF into the Olga Basin (Figure 1b). We first present the recent Nansen Legacy observations (2019–2022), followed by the historical data dating back to 1950.

4.1. Hydrography and Circulation South of the Polar Front From Recent Observations (2019–2022)

The inflow into the southern part of the Hopen Trench mainly consists of AW between the surface and 50–100 m above the seafloor (Figure 3, Sections B–H). The surface temperature core is centered above the deepest part of the trough and the salinity core is above the northwestern slope of the Central Bank. The absolute geostrophic current (u_g) estimate suggests two dynamical cores flowing northeastward along the northwestern slope of the Central Bank (Figure 4, Section H). One branch is located on the upper slope above the 300 m isobath, and one smaller in magnitude on the lower slope close to the center of the trough. This bifurcation is likely a result of diverging bathymetry south of Section H, and is also seen in the depth-averaged currents (Figure 4b).

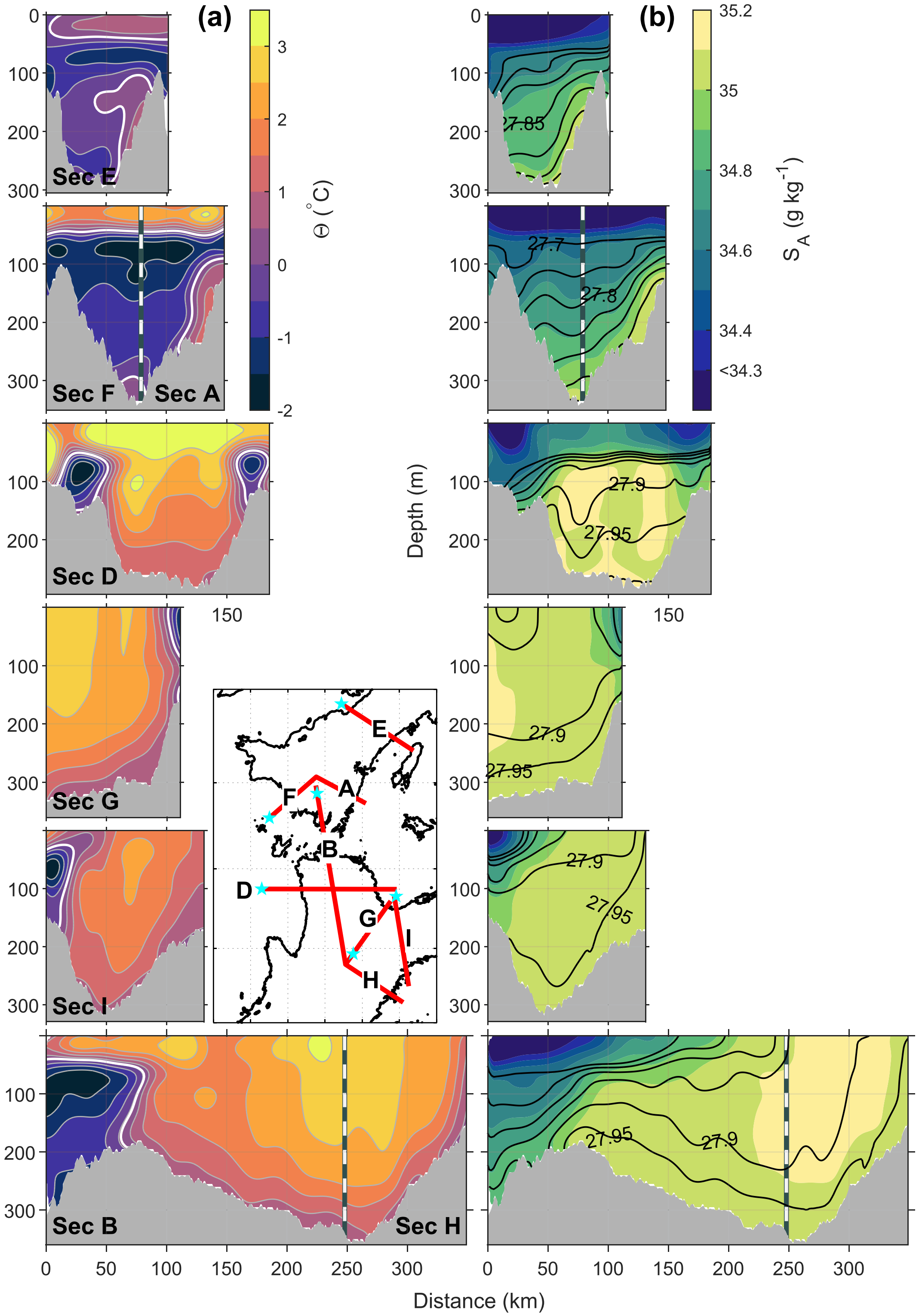

Figure 3. Hydrographic cross-sections of (a) Conservative Temperature, Θ, and (b) Absolute Salinity, S_A, along the sections defined in Figure 2b, also indicated on the map insert here. Horizontal distance is referenced to the edge of the section, marked by blue stars on the map. Sections F-A and B-H are joined at the location marked by the vertical bars. White line in (a) is the 0.1°C isotherm. Black contours in (b) show isopycnals at every 0.05 kg m^{-3} interval, starting at 27.7 kg m^{-3}. The analysis period covers the months from August to February between 2019 and 2022.

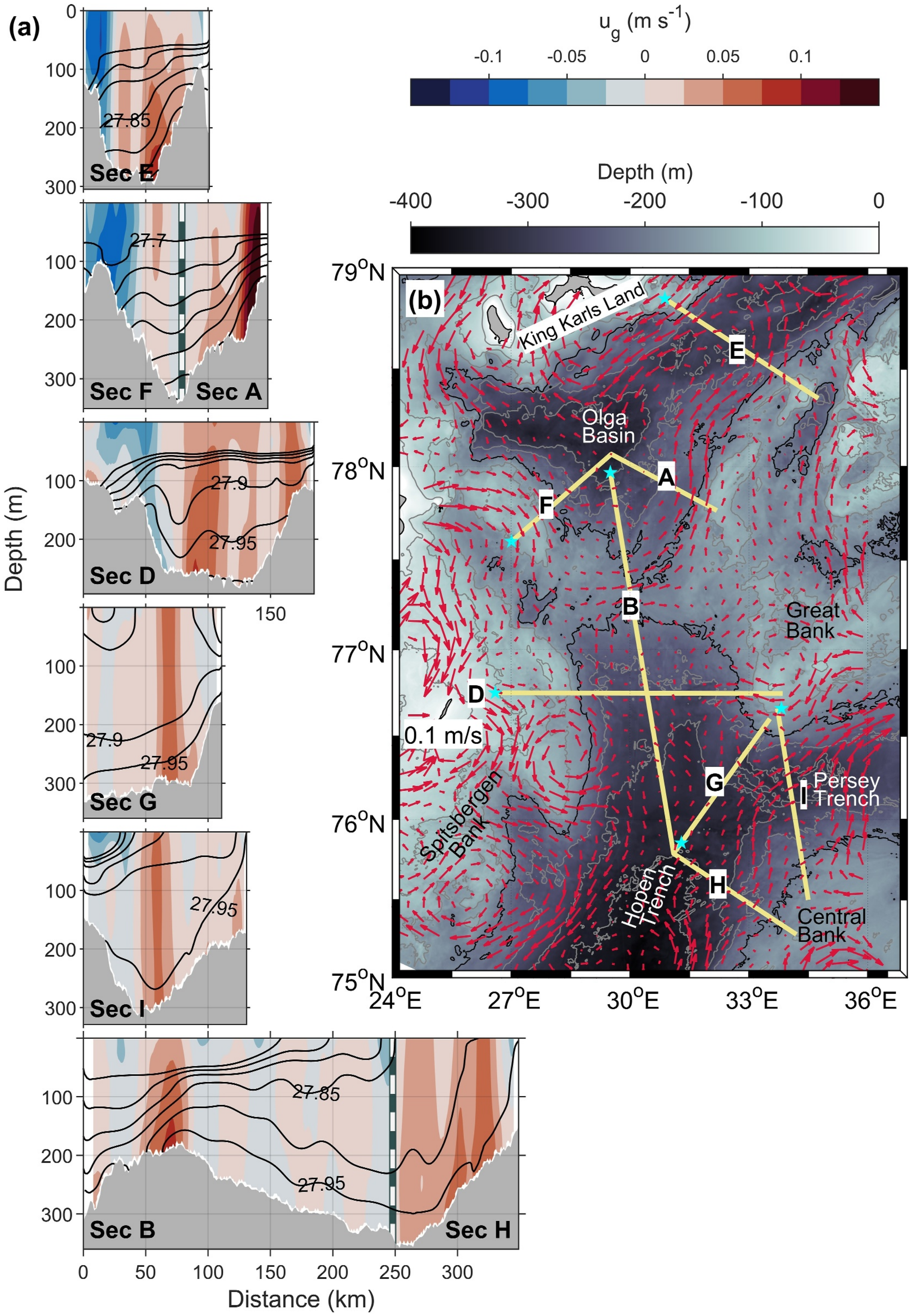

Figure 4. (a) Absolute geostrophic velocities, u_g, normal to the sections marked in (b). 0 km is the edge of the section as marked by the blue star in (b). Positive velocities are directed into the page. Black contours in (a) show isopycnals at every 0.05 kg m^{-3} interval, starting at 27.7 kg m^{-3}. (b) Objectively mapped, divergence-free, depth-averaged currents from SADCP, LADCP and glider DAC. Gray lines are isobaths drawn at every 50 m from 50 to 300 m depth. Black line is the 200 m isobath. Data included covers the months from August to February between 2018 and 2022.

Table 3
Volume Transport, V_{u_g} (in Units of Sv), for the Selected Water Masses and the Total Transport, Through the Different Composite Sections

Sec.	AW	mAW	wPW	PW	Total V_{u_g}
H	0.6	0.3	0.1	–	0.9
I	0.0	0.3 (−0.1)	0.2	0.0	0.5 (−0.2)
G	0.2	0.1	0.2	0.0	0.5
D	0.2	0.3	0.1	0.1 (−0.1)	0.9 (−0.3)
B(PF)	–	–	0.1	0.2	0.3
A	–	0.1	0.2	0.2	0.5
F	–	–	0.1	0.1 (−0.3)	0.1 (−0.5)
E	–	–	0.1	0.3 (−0.3)	0.5 (−0.3)

Note. All transport estimates are calculated from the u_g fields in Figure 4a and rounded to the nearest decimal. Transport estimates are positive and negative (in parentheses), corresponding to positive or negative u_g. Volume transport errors are always less than 0.1 Sv, and typically around 0.05 Sv (Section 3.3).

The total volume transport along the northwestern Central Bank slope (Section H) is 0.9 Sv, divided equally among the branches. Of this, 0.6 Sv is identified as AW (Table 3). The mean temperature of the AW inflow is 2.4 and 2.6°C in the branches on the upper and lower slope, respectively. The mean salinity is 35.11 g kg^{-1} for both branches.

The AW inflow is enveloped by modified AW (mAW) and warm Polar Water (wPW) on the shallow bank and at depth (Figures 5a and 6c, bottom panel). Modified AW is AW cooled below 2°C, while wPW is a mixture of AW and PW (see water mass definitions in Table 2 and in the $\Theta - S_A$ diagram in Figure 5a). AW reaching the northwestern slope of the Central Bank is transformed through cooling by the atmosphere and entrainment of fresher and/or colder water masses (Figure 5a). However, the lack of a clear mixing line between AW and Arctic-origin waters (PW and cBSDW) suggests that transformation through atmospheric cooling is the dominant process (Figure 5a). Continuing from the northwestern slope of the Central Bank, the Atlantic-origin inflow splits into two branches, one continuing east through the Persey Trench and one continuing north along the Hopen Trench (Figure 4b).

The branch continuing along the northern slope of the Central Bank, through the Persey Trench, is cooled and freshened. The AW core subducts, forming a subsurface Θ maximum above the Central Bank slope (Figure 3a,

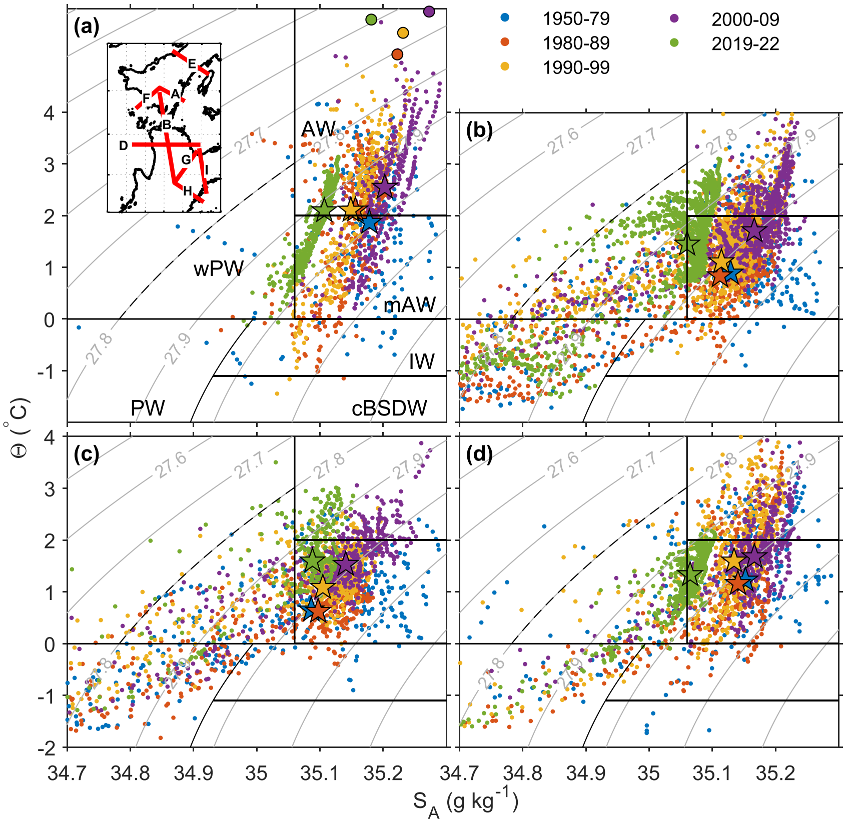

Figure 5. Θ-S_A diagram for (a) Section H, (b) Section B, (c) Section D, and (d) Section I, including historical and recent data collected between August and February. Contours are σ_0 at 0.1 kg m^{-3} intervals. The upper 50 m of the water column is excluded to remove the short-term variability from atmospheric forcing. Stars show the median value for the time periods indicated by the colors. For reference, an inset map showing the section locations is included in (a). Large circles in (a) show annual mean properties in the BSO between the 50 and 200 m layer averaged over the same periods. BSO data are from the ICES Report on Ocean Climate (IROC, https://ocean.ices.dk/core/iroc).

Section I). The core of the eastward current (positive u_g) is located closer to the center of the trench than the AW core, and is bounded by westward flowing currents to the north and weak eastward flowing currents to the south (Figure 4a, Section I). While the AW transport through Section I is insignificant, the eastward transport of mAW and wPW is 0.5 Sv in total (Table 3). On the northern side of the Persey Trench, a surface-intensified westward current transports 0.1 Sv of mAW (Table 3). We note however, that the currents at the section edges may not be fully captured.

The branch flowing northward along the Hopen Trench is confined between the Spitsbergen Bank and the Great Bank, and eventually reaches the sill separating the Atlantic domain in the Hopen Trench from the Polar domain in the Olga Basin. At Section G, an intensified current directed northwest is located at the 300 m isobath (Figure 4a, Section G), approximately 30 km upslope of the AW core (Figure 3, Section G). The variability of this current is discussed further in Section 5.1. The total northward volume transport through Section G is 0.5 Sv, of which 0.2 Sv is AW (Table 3).

Further north, along Section D, the inflowing AW is surrounded by PW on both sides (Figure 3, Section D). Of the total northward volume transport of 0.9 Sv, the Atlantic-origin waters amount to 0.6 Sv (Table 3). On the western edge of the section, a cold core current transports 0.3 Sv southward.

The northward flowing Atlantic-origin waters in the Hopen Trench show a two-branch structure, with the warmer core observed in the western branch (Figures 3 and 4a, Section D). This suggests either a more direct pathway for the AW along the western side or less mixing along this particular route. The water masses found along Section D suggest that the water mass transformation at this higher latitude is influenced more by mixing with PW and by sea ice melt than by atmospheric cooling, in contrast to Section H (Figure 5c).

At the northern edge of the Hopen Trench, a sill (180 m depth) separates the AW domain in the south from the PW domain in the Olga Basin in the north (Figure 3a, Section B). The inflowing Atlantic-origin waters meet the PW at the sill, generating the PF. The sloping isopycnals across the PF set up a bottom-intensified geostrophic flow transporting Atlantic-origin waters (wPW) and PW eastward along the sill (Figure 4a, Section B). The eastward transport along the sill is 0.3 Sv and the flow is largely topographically steered. The part of the current north of the sill continues northeast along the slope of the Great Bank, while the part south of the sill likely recirculates southeast (Figure 4b). Hence, the location and properties of the frontal current govern the amount of Atlantic-origin waters entering the Olga Basin, with a broader (extending further north) and/or stronger flow enabling more Atlantic-origin waters to cross the sill and subduct below the PW.

4.2. Hydrography and Circulation North of the Polar Front From Recent Observations (2019–2022)

The Olga Basin, north of the sill, is dominated by PW and the circulation is cyclonic, following the basin slopes (Figure 4b). PW enters the basin from the north, on either side of King Karls Land (Figure 4b). The coldest waters are located between the 50 and 100 m layer, extending to about 150 m depth at the center of the basin (Figure 3, Sections F, A, and E).

The total southeastward volume transport across Section F is 0.5 Sv, of which 0.3 Sv is PW (Table 3). Parts of this current continue south as the East Spitsbergen Current toward Section D, forming the western reverse flow through Section D and the anticyclonic flow around the Spitsbergen Bank, while parts continue east along the edge of the Olga Basin, toward Sections A and E. The transport through Section A is 0.5 Sv, of which 0.2 Sv is PW. While AW is not present north of the sill, both mAW and wPW are results of Atlantic-origin waters flowing northward toward the sill, further cooled and freshened through interaction with the atmosphere and PW at the PF near the sill. The AW signature north of the PF is manifested as the subsurface temperature and salinity local maximum core hugging the eastern slope of the Olga Basin (Figure 3, Sections A and E). The corresponding eastward volume transport of these Atlantic-origin waters is 0.3 Sv (mAW and wPW) and 0.1 Sv (wPW) through Sections A and E, respectively.

At the northernmost Section E, the eastward volume transport out of the Olga Basin is on the eastern slope (0.5 Sv, where 0.3 Sv is PW). On the northern side of Section E, 0.3 Sv of PW is transported into the Olga Basin. Note however that this inflow of PW from the northeast is warmer and saltier than the PW inflow from the northwest, found along Section F. This is likely due to Atlantic-origin waters entering the Barents Sea from the north along the deepest troughs, in addition to Atlantic-origin waters from the south recirculating in the basin (Figure 3 and Table 4).

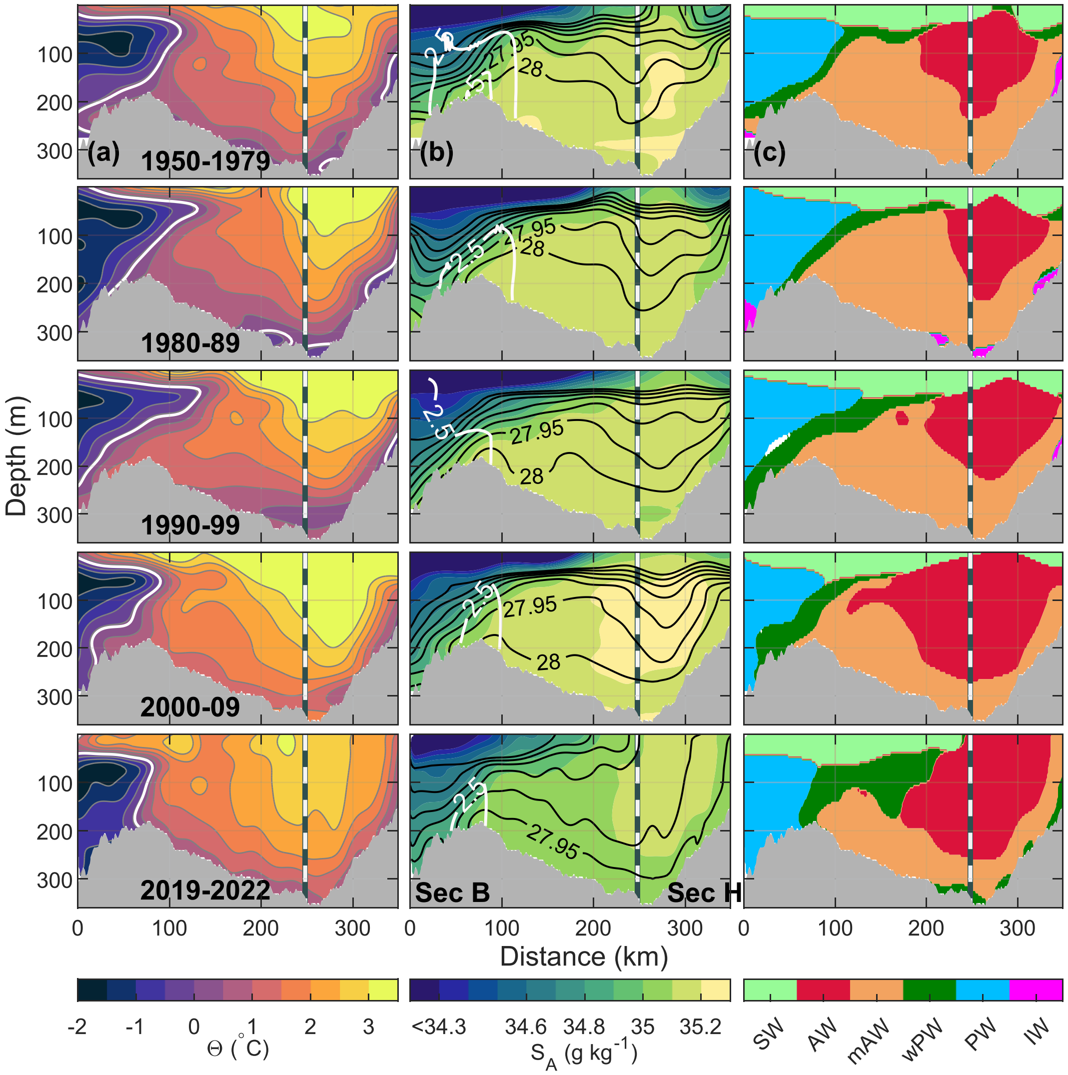

Figure 6. Section B and H hydrography from historical data, averaged over the years indicated in the left panels, only including profiles collected within the months August to February. (a) Conservative Temperature, Θ, (b) Absolute Salinity, S_A, and (c) water masses as defined in Table 2. The white line in (a) is the 0.1°C isotherm, indicating the PF. Black contours in (b) show isopycnals at every 0.05 kg m^{-3} interval starting at 27.7. The white contours in (b) show the relative geostrophic velocity in cm s^{-1}, referenced to the surface. Positive values are directed into the page (east).

4.3. Decadal Changes South of the Polar Front

Between 1980 and 2010 the temperature of the AW inflow into the region increased (Figures 6–8, and Table 4). Nevertheless, the period between 1950 and 1979 stands out as saltier and warmer than the following 80s in most places south of the PF.

The average temperature of AW inflow into Section H was 2.7°C in 1950–1979, increasing to a maximum of 3.5°C in the 2000s (Table 4). The increase in temperature is a combined result of warmer inflow through the BSO and reduced atmospheric cooling over the Barents Sea. The fraction of mAW reduced from about 40% before the 90s to less than 30% in the 2000s (Figure 6c and Table 4). The corresponding AW fraction increased from 40% to 70% in the same period. This transition toward more AW from before the 90s to the 2000s is observed in all sections south of the PF (Table 4), and particularly in Sections B and D. The average temperature on the Atlantic side of the front increased by 0.8°C between 1950 and 2010 in Section H, and by 0.5, 0.6, and 0.3°C in Sections B, D, and I, respectively. This difference in increased temperature between different sections south of the PF is likely

Table 4
Average Water Mass Properties Within Defined Sections in Different Analysis Periods

	AW			mAW			wPW			PW		
Year	$\overline{\Theta}$	$\overline{S_A}$	A	$\overline{\Theta}$	$\overline{S_A}$	A	$\overline{\Theta}$	$\overline{S_A}$	A	$\overline{\Theta}$	$\overline{S_A}$	A
Section H												
1950–1979	2.7	35.17	40	1.0	35.17	43	2.0	35.01	5	–	–	0
1980–1989	2.8	35.15	43	1.0	35.12	37	1.2	35.02	3	–	–	0
1990–1999	3.0	35.16	53	1.0	35.12	35	–	–	0	–	–	0
2000–2009	3.5	35.20	70	1.3	35.17	27	–	–	0	–	–	0
2019–2022	2.5	35.11	64	1.5	35.08	30	0.8	35.05	7	–	–	0
Section B												
1950–1979	2.6	35.16	10	1.2	35.15	44	0.8	35.01	9	−0.9	34.64	22
1980–1989	2.4	35.14	4	1.1	35.14	49	0.8	34.99	8	−1.0	34.55	26
1990–1999	2.5	35.15	9	1.3	35.13	41	0.8	34.95	15	−0.7	34.49	20
2000–2009	2.7	35.18	27	1.7	35.16	32	0.7	34.95	10	−0.8	34.59	17
2019–2022	2.5	35.09	19	1.4	35.08	25	1.7	35.01	20	−1.0	34.71	20
Section D												
1950–1979	–	–	0	1.0	35.15	48	0.8	34.98	14	−0.8	34.69	21
1980–1989	–	–	0	0.9	35.11	47	0.6	34.98	12	−0.9	34.62	24
1990–1999	–	–	0	1.3	35.13	41	0.8	34.95	17	−0.8	34.47	26
2000–2009	2.2	35.14	12	1.7	35.15	43	0.9	34.97	12	−0.7	34.63	14
2019–2022	2.5	35.11	19	1.5	35.10	32	1.1	34.98	9	−0.8	34.72	13
Section I												
1950–1979	2.4	35.16	16	1.2	35.17	51	0.9	35.00	10	−0.4	34.83	6
1980–1989	2.5	35.16	19	1.1	35.14	52	0.8	35.02	6	−0.7	34.79	5
1990–1999	2.7	35.15	31	1.2	35.12	40	1.0	34.99	6	−0.7	34.69	4
2000–2009	2.7	35.18	27	1.4	35.16	49	0.9	34.99	6	−0.3	34.85	1
2019–2022	2.0	35.08	5	1.5	35.08	49	1.2	35.02	36	−0.7	34.78	7
Section F												
2019–2022	–	–	0	–	–	0	0.2	35.00	3	−1.0	34.68	75
Section A												
2019–2022	–	–	0	1.1	35.07	3	0.6	34.98	15	−0.9	34.74	63
Section E												
2019–2022	–	–	0	0.7	35.08	1	0.2	34.92	12	−0.6	34.70	68

Note. Mean Conservative Temperature $(\overline{\Theta})$, Absolute Salinity $(\overline{S_A})$, and percentage of area occupied, A (%) are listed. Errors in the $\overline{\Theta}$ and $\overline{S_A}$ estimates are ±0.1°C and ±0.02 g kg^{-1}, respectively (Section 3.3).

a result of the dynamics in the region, and is discussed in Section 5.2. Note that for Sections B, D, and I, the 80s stand out as the coldest decade (Table 4).

While the temperature of the AW inflow has increased over the decades, the change in salinity is not as pronounced. Both the 80s and 90s indicate a fresher AW and mAW inflow compared to 1950–1979, while the 2000s stand out as anomalously saline (Table 4 and Figure 5). Our recent data (2019–2022), however, show an anomalously fresh AW inflow, with salinity as much as 0.06 g kg^{-1} less than observed in the previous decades (Table 4 and Figure 5a). The freshening is caused by upstream conditioning (Section 5.2) and manifests at all sections south of the PF, where the density in the lower water column tends to be 0.05 kg m^{-3} less than in previous decades (Figures 5, 6b, 7b, and 8b). As a result, the Atlantic-origin waters reaching the sill in the northern part of Section B do not subduct below the PW as readily as in previous decades (Figure 6). The PF is relatively steeper,

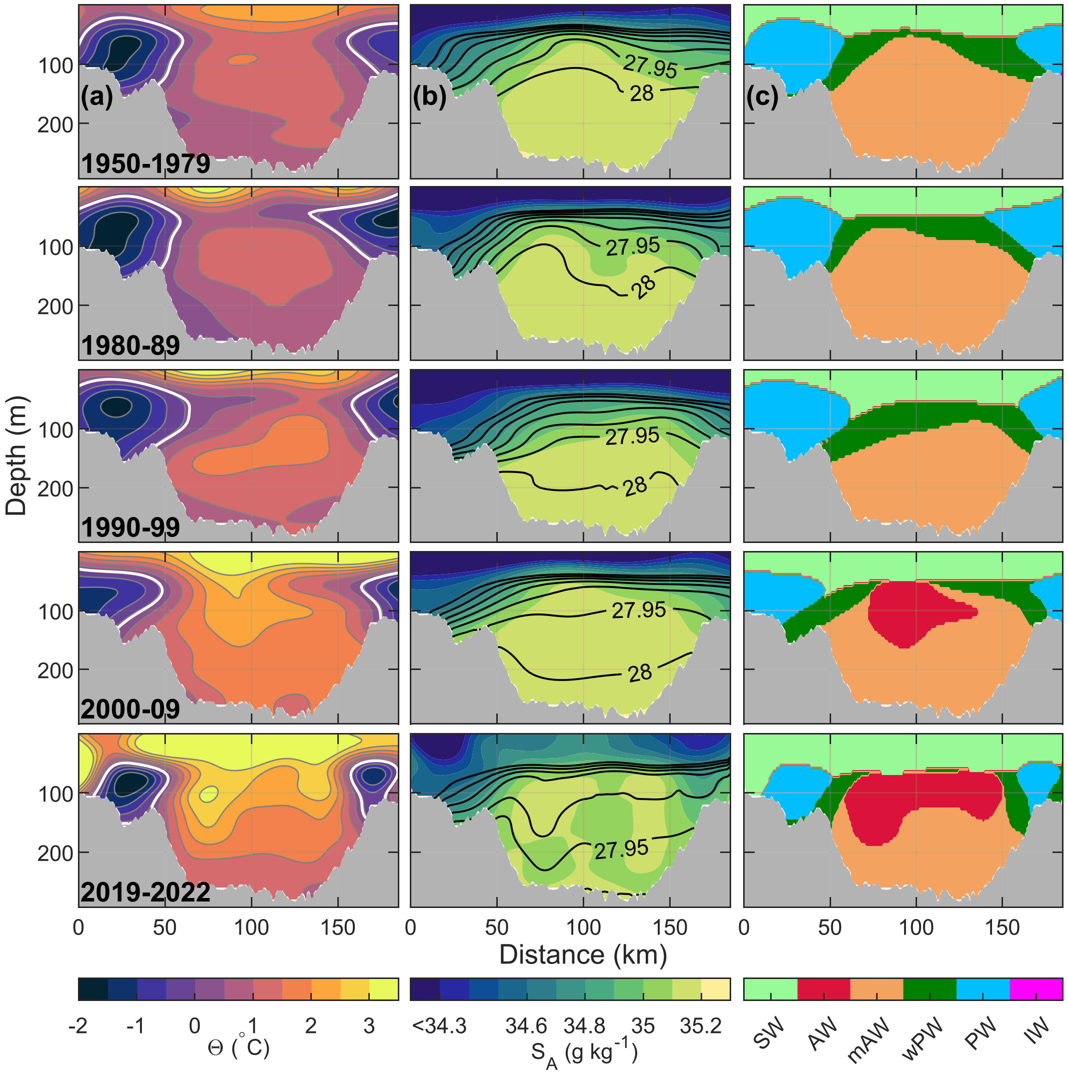

Figure 7. Same as Figure 6 but for Section D.

effectively reducing the amount of Atlantic-origin waters entering the Olga Basin below 100 m depth. In addition, the relative geostrophic flow along the front is weakest in 2019–2022, compared to the previous decades (Figure 6b, white contours). The reduction in the relative geostrophic flow is caused by a decreased density gradient across the front. In addition, decreasing AW density reduces the density of the AW-cold Barents Sea Deep Water (cBSDW) mixing product which is the relatively dense Intermediate Water (IW). IW was observed in different sections before 2000, however, it is absent afterward (Figure 5).

4.4. Decadal Changes North of the Polar Front

PW is the dominant water mass north of the PF in the Olga Basin, on the Great Bank, and along the 100 m isobath on the Spitsbergen Bank (Figures 3 and 9). Here, the Olga Basin is defined as the basin within the 200 m isobath, between 77.4 and 78.5°N and west of 33°E. The largest changes in the distribution of PW between the 50s and the present day can be observed along the Spitsbergen Bank south of 77°N (Figure 9). The area on the Spitsbergen Bank occupied by waters colder than 0.1°C (averaged over the 50–100 m layer) was about 20×10^3 km^2 between 1950 and 1979, while only 12×10^3 km^2 in the 2000–2009 period (Figure 9a). The corresponding change in the average temperature for the same area was an increase from −0.7 ± 0.1°C to −0.4 ± 0.1°C. This reduction in the area occupied by Arctic-origin waters is likely a result of the increased temperatures of the Atlantic-origin waters,

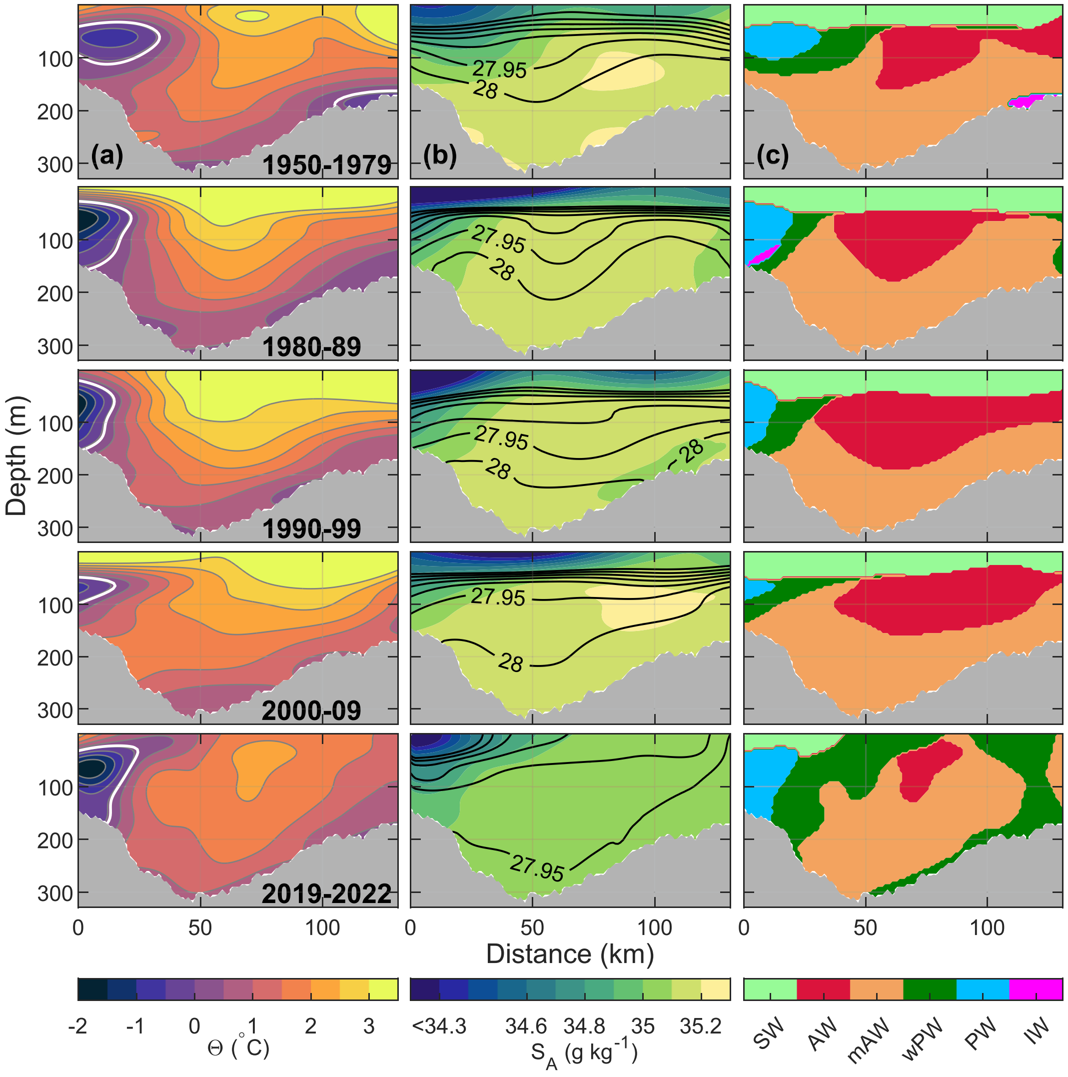

Figure 8. Same as Figure 6 but for Section I.

flowing in on both the eastern and western sides of the Spitsbergen Bank (Figure 9a). Below 100 m depth on the Spitsbergen Bank, the average temperature increased even more than that within the 50–100 m layer. From the 1980s to 2000s, the average temperature below 100 m depth increased from −0.6 ± 0.1°C to −0.1 ± 0.1°C, suggesting a larger AW influence at depth.

In the Olga Basin, the 80s and 90s are the coldest and warmest decades, respectively. However, temperature variations are small in the 50–100 m layer where average temperatures range between −1.4 ± 0.1°C and −1.3 ± 0.1°C (Figure 9a and Table 5). The average salinity, on the other hand, exhibits larger variations where the 90s stand out as particularly fresh with an average salinity of 34.41 g kg^{-1} in the 50–100 m layer (Figure 9b). As a result, the average density in the 50–100 m layer, which mainly consists of PW, is 27.56 kg m^{-3} in the 90s, as much as 0.07 kg m^{-3} less than any other decade. Below 100 m depth, temperature variations are much larger than in the upper layer, likely as a result of varying Atlantic-origin water inflow. In the same depth, average salinity varies only little (Figure 10b and Table 5). The main pathway of Atlantic-origin waters is visible as relatively warm water following the 200 m isobath along the basin (Figure 10a). From the 80s to the 2000s, the average temperature below 100 m depth increased from −0.5 ± 0.1°C to 0 ± 0.1°C (Table 5). The Olga Basin, below 100 m depth, was at its warmest in the 90s when the average temperature was 0.2 ± 0.1°C. Note that the

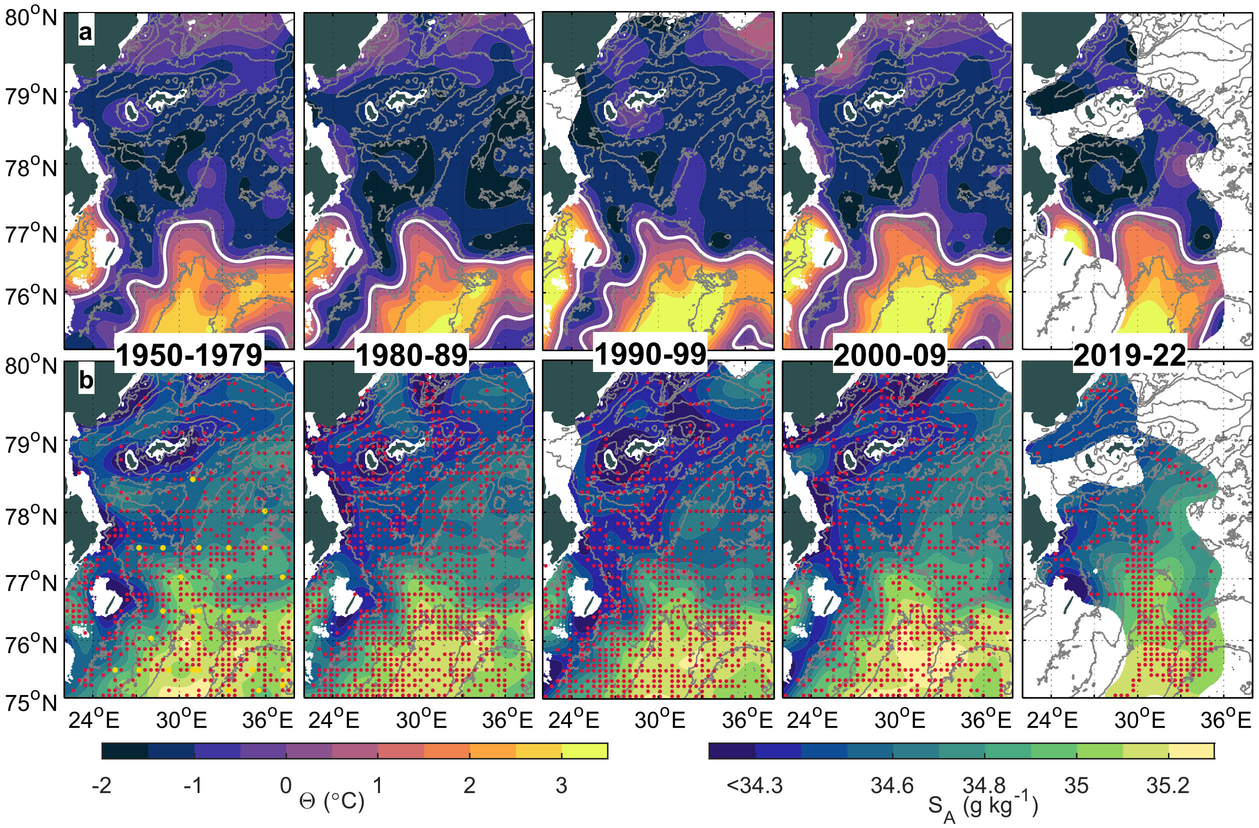

Figure 9. (a) Conservative Temperature, Θ, and (b) Absolute Salinity, S_A, averaged over the 50–100 m layer and objectively mapped for the different time periods as described in Section 3.4. Only profiles within the period August to February are included. Red dots in (b) indicate 10 by 10 km bins where we have data. Yellow dots in the 1950–1979 panel indicate where we have binned profiles that cover the water column deeper than 100 m.

objectively mapped temperature and salinity fields below 100 m depth are not presented for the 1950–1979 period as there were few CTD profiles that covered the entire water column during that time (yellow dots in Figure 9b).

On the Great Bank, defined as the region above the 200 m isobath between 76° and 77°N and east of 33°E, the 80s stand out as colder and fresher than the previous 1950–1979. The average temperature and salinity in the 80s were −1.4 ± 0.1°C and 34.68 ± 0.02 g kg^{-1}, respectively, within the 50–100 m layer (Figure 9). After the 80s, temperatures increased both in the 50–100 m layer and below 100 m depth, and peaked in the 2000s. The increased layer-averaged temperature on the Great Bank in the 2000s coincides with a broadening of the PF region on the sill at the northern edge of the Hopen Trench (Figure 9). Atlantic-origin waters flow further east onto the Great Bank in the 2000s and in recent observations (2019–2022) than in previous decades.

Table 5
Average Properties in the Olga Basin

	50–100 m layer			Below 100 m		
Year	$\overline{\Theta}$	$\overline{S_A}$	$\overline{\sigma_0}$	$\overline{\Theta}$	$\overline{S_A}$	$\overline{\sigma_0}$
1950–1979	−1.4	34.55	27.68	–	–	–
1980–1989	−1.4	34.50	27.63	−0.5	34.82	27.85
1990–1999	−1.3	34.41	27.56	0.2	34.80	27.80
2000–2009	−1.4	34.51	27.63	0.0	34.82	27.83
2019–2022	−1.4	34.59	27.70	−0.5	34.80	27.84

Note. The Olga Basin is here defined as the basin within the 200 m isobath, between 77.4 and 78.5°N and west of 33°E. Mean Conservative Temperature $(\overline{\Theta})$, Absolute Salinity $(\overline{S_A})$ and potential density anomaly $(\overline{\sigma_0})$ for different analysis periods are listed. Errors in the $\overline{\Theta}$ and $\overline{S_A}$ estimates are ±0.1°C and ±0.02 g kg^{-1}, respectively, calculated as described in Section 3.3.

5. Discussion

5.1. Atlantic Water Pathways in the Western Barents Sea

The main AW path into the Barents Sea is through the Bear Island Trough. Excluding the Norwegian Coastal Current, the annual mean inflow is 2 Sv, and 2.1 Sv when averaged over August to February (Smedsrud et al., 2010). A fraction of the inflow recirculates and leaves the Barents Sea as a westward flowing current south of the Bear Island (Gawarkiewicz & Plueddemann, 1995; Skagseth, 2008; Smedsrud et al., 2010). The volume transport of the westward current is 1.2 Sv; however, how much of this is recirculating AW and how much is Arctic-origin water is not known (Gawarkiewicz &

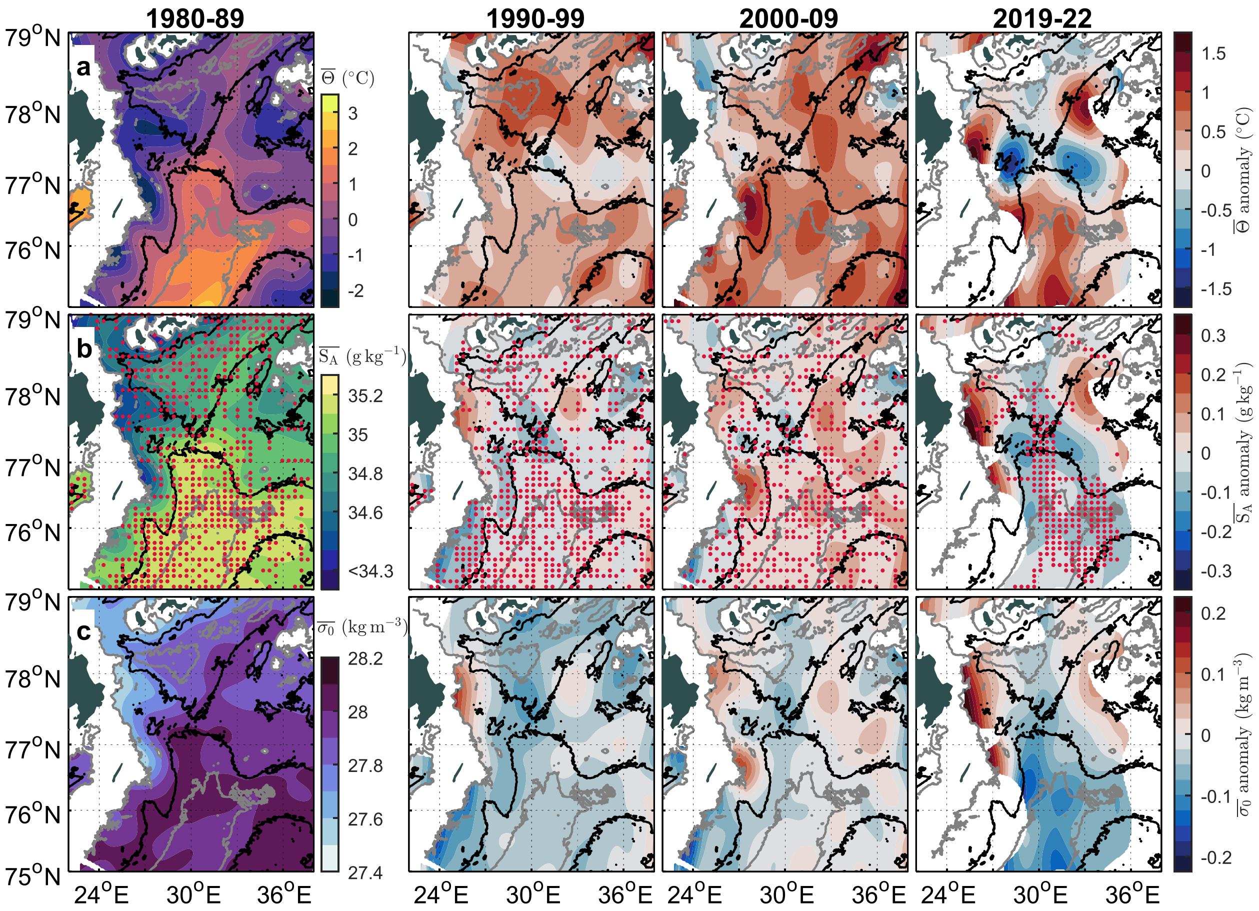

Figure 10. Average (a) temperature, $\overline{\Theta}$, (b) salinity, $\overline{S_A}$ and (c) potential density anomaly, $\overline{\sigma_0}$ for the time period 1980–1989, below 100 m depth. For the following time periods, temperature, salinity and density anomalies relative to the 80s are displayed in the respective rows. Only profiles within the period August to February are included. Red dots in (b) indicate 10 by 10 km bins where we have data. Black line is the 200 m isobath while gray lines show the 100 and 300 m isobaths.

Plueddemann, 1995; Smedsrud et al., 2010). In Figure 11, we summarize the inferred pathways and volume transport estimates from the observations synthesized in this study. We observe the inflow at the southeastern part of the Hopen Trench (Section H) to be 0.9 ± 0.1 Sv, suggesting that half of the AW inflow through the BSO reaches the Hopen Trench (Table 3 and Figure 11).

Between the Hopen Trench and the Central Bank (Section H), the current divides at the 300 m isobath (two velocity cores are observed, see Figure 4 Section H) where the shallower branch continues into the Persey Trench (0.5 Sv), while the deeper branch continues northward (0.6 Sv). Between the Hopen Trench and the Great Bank (Section G), the absolute geostrophic velocity core flows northwestward, centered at the 300 m isobath, co-located with a local surface temperature maximum (Figures 3a and 4a, Section G). This is contrary to the observations made by Våge et al. (2014), where they observed currents flowing southeast in nearly the same location during a week in August 2007. Our absolute geostrophic velocity fields are based on three glider transects conducted during December and January, and one reason for the discrepancy could be a seasonal change (Figure 2). In fact, our objectively mapped currents based on SADCP, LADCP and glider DAC do suggest that currents at times flow southeast across Section G (Figure 4b). Furthermore, this is a region where tidal currents may exceed 20 cm s^{-1} (Fer & Drinkwater, 2014). Extracting the mean flow of <10 cm s^{-1} through detiding of individual SADCP transects and LADCP profiles may have uncertainties with comparable magnitude and must be interpreted with caution. In addition, Våge et al. (2014) states that the circulation south of the PF in the Barents Sea is too complex to be conclusively described by individual surveys, as sea level, tidal flows and winds change the dynamics of the front.

Between the Spitsbergen Bank and the Great Bank (Section D), we observe a four-branch structure, three branches flowing northward and one branch flowing southwards (Figure 4a). The branches on either side, located

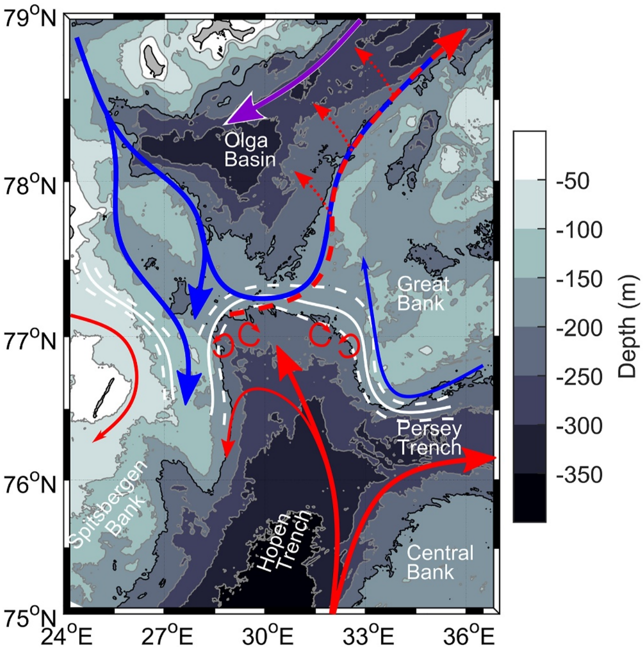

Figure 11. Mean currents of Atlantic Water (red) and Polar Water (blue and purple) in our study region, as inferred from our observations between 2019 and 2022. Red dashed line indicates subducted Atlantic-origin waters. Purple line is PW that is relatively warmer than PW in the west, due to mixing with deep AW inflow from north. White solid line marks the mean position of the Polar Front based on historical and recent data, with one standard deviation envelope (dashed).

on the shelves, mainly carry Arctic-origin water, whereas PW flows north on the Great Bank shelf, and south on the Spitsbergen Bank (Figures 3 and 4a). The two branches in the Hopen Trench consist of Atlantic-origin waters, and are hereby referred to as the western and eastern branches of Section D (Figures 3 and 4). The volume transport estimates of the western and eastern branches are 0.5 and 0.2 Sv, respectively. Hence, the total northward transport by these two branches is 0.7 Sv, which exceeds the transport estimates between Hopen Trench and Great Bank (Section G) and the branch on the slope of the Central Bank (lower branch of Section H). This suggests the northward transport is not fully captured by Section H and G. Note that there is a seasonal difference in our data coverage along Section D (between the Spitsbergen Bank and the Great Bank) compared to Section H and G: we only collected data along Section D during the October cruises, whereas the gliders retrieved data along Section G and H mainly during late fall and winter (Figure 2 and Table 1). However, since AW inflow is expected to be greater in late fall and winter compared to October (Smedsrud et al., 2010), the observed discrepancy between the flow between the Spitsbergen Bank and the Great Bank (Section D) and the flow between the Hopen Trench and the Central Bank (Sections H) and between the Hopen Trench and the Great Bank (Section G) is likely not due to seasonality.

Our observations show that the branch along the Spitsbergen Bank (western branch in Section D) is warmer than the eastern one, suggesting a relatively direct route, or less mixing along the route compared to the flow between the Hopen Trench and the Great Bank (Section G). Therefore, we hypothesize that the branch along the western slope of the Great Bank (eastern branch in Section D) is a continuation of the branch observed between the Hopen Trench and the Great Bank (Section G) and that the branch on the slope of the Spitsbergen Bank (the western branch in Section D) is a continuation of the waters flowing northward along the deeper slope of the Central Bank (outer core in Section H), and farther along the sill (Section B). Barton et al. (2018) suggest that AW flows clockwise around the Hopen Trench due to potential vorticity constraints in a basin with a shallower northern outflow than inflow. This could be true for the Hopen Trench where Atlantic-origin waters entering from the south eventually flow across the sill at the northern edge of the Hopen Trench and continue into the Olga Basin. Hence the western branch in Section D may originate from the AW flowing north in the outer core observed in Section H. It shifts from following the eastern slope to the western slope to conserve its potential vorticity as the water depth decreases. The dynamics involved in this transition require further study.

Another possibility is that this branch between Spitsbergen Bank and Great Bank (western branch in Section D) comes from a retrograde current flowing northeast along the Spitsbergen Bank slope such as described by Loeng (1991) and Li and McClimans (1998). While our three SADCP transects across the Spitsbergen Bank slope would contradict this (Figures 2b and 4b) we cannot exclude this as a possibility. Nevertheless, such a retrograde current is unlikely to follow the Spitsbergen Bank from the BSO as several studies report westward flowing currents along the southern Spitsbergen Bank (Gawarkiewicz & Plueddemann, 1995; Parsons et al., 1996; Skagseth, 2008).

Once reaching the sill between the Hopen Trench and the Olga Basin, the branches flowing north between the Spitsbergen Bank and the Great Bank have different outcomes. The eastern PW branch likely continues north along the Great Bank. The western and eastern branches of Atlantic-origin waters interact with the front, mix with PW and eventually subduct, partly contributing to the frontal current flowing northeast along the Olga Basin slope, and partly recirculating along the slope of the Spitsbergen Bank.

At the sill, a geostrophic current flowing eastward develops due to the density difference between the AW and PW (Figure 4, Section B and Figure 6b). We observe a decrease in the relative geostrophic velocity along the front over recent decades (Figure 6b). These changes to the frontal current are caused by the decadal changes of the PW and AW (discussed in Section 5.2). A weakening and narrowing of the geostrophic current at the front suggests a reduction of the amount of Atlantic-origin waters reaching the northern side of the sill in the Olga Basin. The PF is a site for rapid mixing between Atlantic-origin waters and Arctic-origin waters. The dynamics of the PF and the frontal current are discussed in Kolås et al. (2024) and will not be addressed in depth here. The frontal jet observed during our 2019–2022 observations continues toward Section A and E (eastern side of the Olga Basin) where the temperature signature of Atlantic-origin waters is still present. Model studies, such as Aksenov et al. (2010), support the flow of Atlantic-origin waters across the sill at the northern edge of the Hopen Trench.

5.2. Decadal Change in Temperature and Salinity

Between 1980 and 2010 we observe a warming of the AW along all sections south of the PF (Table 4 and Figures 6–8). Correspondingly, the area occupied by AW is expanding, in agreement with findings reported in numerous studies (Årthun et al., 2012; Barton et al., 2018; R. B. Ingvaldsen et al., 2021; Onarheim et al., 2014; Oziel et al., 2016; Skagseth et al., 2008; Smedsrud et al., 2010). The area occupied by AW has increased because regions previously containing mAW are now filled with AW. This is caused by a temperature increase in the AW inflow and a less efficient cooling of the ocean by the atmosphere in the Barents Sea (Skagseth et al., 2020). Time series show an increase in AW and surface temperatures across the BSO since the 80s (Barton et al., 2018; Skagseth et al., 2008). As a result, the PF position defined by the 0.1°C isotherm has shifted about 50 km north after the 90s (Figure 6). In addition, the temperature gradient across the PF, here calculated as the mean gradient in the 100–180 m depth-layer between ±60 km of the highest point on the sill (between 18 and 138 km in Figure 6), increased from 1.8°C/100 km to 2.5°C/100 km between the 90s and the 2019–2022 period. However, the change in the PF position is not only a result of increased AW temperatures but also closely linked to the density difference between the AW south of the front and PW to the north, determined by temperature and salinity differences.

From the 80s to the 90s, the temperature of Atlantic-origin waters south of the PF increased (Table 4), without changing the position of the front. Instead, more Atlantic-origin water flowed under the PW into the Olga Basin, and the across-front gradient of layer-averaged temperature decreased by 0.3°C/100 km from the 80s to the 90s (Figures 9 and 10). The increased flow of Atlantic-origin water across the PF was likely a result of anomalously fresh PW north of the PF within the Olga Basin in the 90s (Table 5). As a result, the layer-average density gradient across the PF increased from 0.18 kg m^{-3}/100 km to 0.21 kg m^{-3}/100 km. The fresh PW layer in the Olga Basin in the 90s is supported by observations by Lind et al. (2018). We speculate that this contributed to the record-warm waters below 100 m depth in the Olga Basin observed in the 90s.

In the 2000s, AW reached record-high temperatures and salinity south of the PF. However, as the PW in the Olga Basin also had a higher salinity in the 2000s compared to the 90s, the layer-averaged across-front density gradient was reduced by 0.04 kg m^{-3}/100 km compared to the 90s. Consequently, less Atlantic-origin waters flowed under the PW into the Olga Basin. Instead, the AW inflow was directed east onto and along the Great Bank (Figures 9 and 10). The core of the relative geostrophic frontal current was stronger and located further south in the 2000s compared to the 90s, supporting an eastward shift of the Atlantic-origin waters (Figure 6b).

The AW inflow in the 2019–2022 period was anomalously fresh. This is due to upstream conditions and is also observed in the annual mean properties of the AW inflow through the BSO (Figure 5a). The low-salinity anomaly in the AW inflow is connected to the largest freshening event in 120 years in the North Atlantic and can be traced along the Norwegian coast (Holliday et al., 2020). Time-averaged properties in the 50–200 m layer in the BSO in the 2019–2022 period is about 0.05 g kg^{-1} fresher than during the 80s and 90s, and nearly 0.1 g kg^{-1} fresher than during the 2000s (Figure 5a). As a result, the AW south of the PF is about 0.05 kg m^{-3} less dense than in previous decades (Figure 6), and the layer-average density gradient across the PF is reduced to 0.10 kg m^{-3}/100 km. Consequently, the amount of Atlantic-origin waters extending northward under the PW across the PF is reduced (Figures 6 and 10). If the temperature of the AW inflow continues to increase without an increase in AW salinity to compensate for the density loss, we expect that less Atlantic-origin waters will be able to cross the PF. In addition, even if the Atlantification of the Olga Basin continues as speculated by Lind et al. (2018), we hypothesize that an increased salinity in the Olga Basin will serve as a negative feedback mechanism, slowing down the Atlantification by further reducing the density gradient across the PF.

Another effect of the anomalously fresh AW inflow is the reduced dense and intermediate water production. Atlantic-origin waters reaching the PF from the south are warmer as a result of reduced cooling of AW by the atmosphere in the Barents Sea. These warmer waters mix with cBSDW. Until 2018, the increased AW temperature was largely compensated for by increased salinity (Skagseth et al., 2020) with respect to density. The recent freshening of the AW causes water masses produced by mixing AW with cBSDW to be less dense (Figure 5). This was previously suggested by Skagseth et al. (2020) and may have consequences for the general dense water production in the Barents Sea.

6. Summary

We presented the hydrography and circulation in the northwestern Barents Sea. Observations from three scientific cruises and nine glider missions conducted in the Barents Sea between 2019 and 2022 are synthesized to describe the present conditions. In addition, historical data collected after 1950 are averaged over decades and compared to recent observations.

Approximately half of the AW inflow through the Barents Sea Opening reaches the Hopen Trench between Spitbergen Bank and Central Bank, carrying 0.9 ± 0.1 Sv of Atlantic-origin waters (Figures 4 and 11; Table 3). The AW circulation in the Hopen Trench bifurcates; one branch flowing east along the Persey Trench and one continuing north along the Hopen Trench (Figure 11). Each branch transports about 0.5 Sv of Atlantic-origin waters. At the northern edge of the Hopen Trench, Atlantic-origin waters subduct under the PW and the Polar Front (PF), continuing northeastward along the eastern slope of the Olga Basin as a topographically steered current. The AW is modified continuously along its pathway. Upstream of the Hopen Trench, AW transformation is primarily through cooling by the atmosphere, while along the Hopen Trench and the Persey Trench the transformation is mainly driven by mixing between AW and PW (Figure 5).

South of the PF, the average AW temperature increased by 0.7°C from 1980 to 2010. The 100–180 m layer-average temperature gradient across the PF has increased by nearly 40% (from 1.8°C/100 km to 2.5°C/100 km) between the 80s and the 2019–2022 period. In the same period, the layer-average density gradient across the PF was reduced by 50% (from 0.21 kg m^{-3}/100 km to 0.10 kg m^{-3}/100 km).

We hypothesize that the amount of Atlantic-origin waters entering the Olga Basin over the topographic sill is largely governed by a relative geostrophic current, which is established by the density difference between AW south of the sill and PW in the Olga Basin. Our analysis shows that the Olga Basin cooled from the 90s to the 2000s, despite the increasing AW temperatures south of the sill (Tables 4 and 5). This was likely a result of denser waters with increased salinity residing in the Olga Basin. On the other hand, the salinity of the AW inflow into the northwestern Barents Sea decreased by nearly 0.1 g kg^{-1} from the 2000s to the 2019–2022 period, reducing the AW density south of the PF by as much as 0.05 kg m^{-3}. Consequently, the transport of Atlantic-origin waters into the Olga Basin decreased, leading to a continuous decrease of the average temperature below 100 m depth in the Olga Basin (Table 5). Additionally, the mixing of less dense AW with PW in the 2019–2022 period produced relatively less dense water compared to previous decades, which could have implications for the general dense water production in the Barents Sea.

Data Availability Statement

In this study, we used data collected as part of the Nansen Legacy project, all openly available as listed below. This includes hydrographic data from nine glider missions conducted between 2019 and 2022, and ship CTD and MSS data from three research cruises conducted between 2020 and 2022. Glider data in the period August 2019–February 2021 are available from https://doi.org/10.21335/NMDC-381060465 (Kolås et al., 2022) and the period February 2021–October 2022 from https://doi.org/10.21335/NMDC-571158912 (Fer et al., 2024). CTD and MSS data from RV G.O. Sars, collected in October 2020, are available from https://doi.org/10.21335/NMDC-1752779505 and https://doi.org/10.21335/NMDC-239170563, respectively (Fer, Baumann, Elliot, & Kolås, 2023; Fer, Skogseth, et al., 2023). CTD and MSS data from RV Kronprins Haakon, collected in February 2021, are available from https://doi.org/10.21335/NMDC-1544015310 and https://doi.org/10.21335/NMDC-1939445412, respectively (Fer, Baumann, Kalhagen, et al., 2023; Fer, Nilsen, et al., 2023). CTD and MSS data from RV Kristine Bonnevie, collected in October 2022, are available from https://doi.org/10.21335/NMDC-943526062 and https://doi.org/10.21335/NMDC-1169583367, respectively (Fer, Baumann, Hana, et al., 2023; Fer, Baumann, Koenig, et al., 2023). Additional data used are SADCP data from several different Nansen Legacy cruises (Cannaby et al., 2022), historical CTD profiles from the UNIS hydrographic database (Skogseth et al., 2019), bathymetry data from the International Bathymetric Chart of the Arctic Ocean (IBCAO), version 4, available from https://www.gebco.net/data_and_products/gridded_bathymetry_data/arctic_ocean/ and described by Jakobsson et al. (2020), and SST from the product SEAICE_ARC_SEAICE_L4_NRT_OBSERVATIONS_011_008 at 0.05° resolution based upon observations from the Metop_A AVHRR instrument (Copernicus Marine Service, 2019).

Acknowledgments
This work was supported by the Nansen Legacy Project, project number 276730. We thank the officers, crew and scientists of the RV G.O. Sars cruise in October 2020, RV Kronprins Haakon in February 2021 and RV Kristine Bonnevie cruise in October 2022. We thank the glider team at NorGliders (http://norgliders.gfi.uib.no/), for operating and maintaining all the glider missions in challenging conditions in the Barents Sea. An anonymous reviewer and Dr. Emyr Martyn Roberts provided thoughtful comments which helped improve the paper.

References

Aksenov, Y., Bacon, S., Coward, A. C., & Nurser, A. J. G. (2010). The North Atlantic inflow to the Arctic Ocean: High-resolution model study. *Journal of Marine Systems*, *79*(1), 1–22. https://doi.org/10.1016/j.jmarsys.2009.05.003

Årthun, M., Eldevik, T., Smedsrud, L. H., Skagseth, Ø., & Ingvaldsen, R. B. (2012). Quantifying the influence of Atlantic heat on Barents Sea ice variability and retreat. *Journal of Climate*, *25*(13), 4736–4743. https://doi.org/10.1175/JCLI-D-11-00466.1

Årthun, M., Ingvaldsen, R., Smedsrud, L., & Schrum, C. (2011). Dense water formation and circulation in the Barents Sea. *Deep Sea Research Part I: Oceanographic Research Papers*, *58*(8), 801–817. https://doi.org/10.1016/j.dsr.2011.06.001

Barton, B. I., Lenn, Y.-D., & Lique, C. (2018). Observed Atlantification of the Barents Sea causes the Polar Front to limit the expansion of winter sea ice. *Journal of Physical Oceanography*, *48*(8), 1849–1866. https://doi.org/10.1175/JPO-D-18-0003.1

Baumann, T. M., Fer, I., Koenig, Z., Randelhoff, A., Rieke, O., Hana, I., & Årvik, A. (2023). Polar Front Process Cruise 2022: Cruise Report, *The Nansen Legacy Report Series* (Vol. *39*). https://doi.org/10.7557/nlrs.6982

Cannaby, H., Ingvaldsen, R., Reigstad, M., Søreide, J., Gerland, S., Ludvigsen, M., & Fransson, A. (2022). Vessel mounted Acoustic Doppler Current Profiler data collected in the Barents Sea and adjacent Arctic Ocean by the Norwegian research icebreaker R/V Kronprins Haakon, during 7 individual surveys conducted for the Nansen Legacy project [Dataset]. *Institute of Marine Research*. https://doi.org/10.21335/NMDC-1175579976

Copernicus Marine Service. (2019). Arctic Ocean - Sea and ice surface temperature [Dataset]. *E.U. Copernicus Marine Service Information*. Retrieved from https://resources.marine.copernicus.eu/product-detail/SEAICE_ARC_SEAICE_L4_NRT_OBSERVATIONS_011_008/INFORMATION

Fer, I., Baumann, T. M., Elliott, F., & Kolås, E. H. (2023). Ocean microstructure measurements using an MSS profiler during the Nansen Legacy cruise, GOS2020113, October 2020 [Dataset]. *Norwegian Marine Data Centre*. https://doi.org/10.21335/NMDC-239170563

Fer, I., Baumann, T. M., Hana, I., Koenig, Z., Randelhoff, A., Rieke, O., & Årvik, A. (2023). Ocean microstructure measurements using an MSS profiler during the Nansen Legacy cruise, KB2022625, October 2022 [Dataset]. *Norwegian Marine Data Centre*. https://doi.org/10.21335/NMDC-1169583367

Fer, I., Baumann, T. M., Kalhagen, K., Koenig, Z., & Kolås, E. H. (2023). Ocean microstructure measurements using an MSS profiler during the Nansen Legacy cruise, KH2021702, February 2021 [Dataset]. *Norwegian Marine Data Centre*. https://doi.org/10.21335/NMDC-1939445412

Fer, I., Baumann, T. M., Koenig, Z., Randelhoff, A., Rieke, O., Hana, I., & Årvik, A. (2023). Ocean hydrography and current profiles from the Nansen Legacy Process Cruise to the Barents Sea, KB2022625, October 2022 [Dataset]. *Norwegian Marine Data Centre*. https://doi.org/10.21335/NMDC-943526062

Fer, I., Bosse, A., & Dugstad, J. (2020). Norwegian Atlantic slope current along the Lofoten Escarpment. *Ocean Science*, *16*(3), 685–701. https://doi.org/10.5194/os-16-685-2020

Fer, I., & Drinkwater, K. (2014). Mixing in the Barents Sea Polar Front near Hopen in spring. *Journal of Marine Systems*, *130*, 206–218. https://doi.org/10.1016/j.jmarsys.2012.01.005

Fer, I., Kolås, E. H., Brakstad, A., & Elliott, F. (2024). Physical oceanography data from gliders in the Barents Sea, February 2021–October 2022 [Dataset]. *Norwegian Marine Data Centre*. https://doi.org/10.21335/NMDC-571158912

Fer, I., Nilsen, F., Baumann, T. M., Kalhagen, K., Koenig, Z., & Kolås, E. H. (2023). Ocean hydrography and current profiles from the Nansen Legacy Winter Process Cruise to the northern Barents Sea, KH2021702, February 2021 [Dataset]. *Norwegian Marine Data Centre*. https://doi.org/10.21335/NMDC-1544015310

Fer, I., Skogseth, R., Astad, S., Baumann, T., Elliott, F., Falck, E., et al. (2023). Ocean hydrography and current profiles from the Nansen Legacy cruise to the northern Barents Sea, GOS2020113, October 2020 [Dataset]. *Norwegian Marine Data Centre*. https://doi.org/10.21335/NMDC-1752779505

Fer, I., Skogseth, R., Astad, S. S., Baumann, T., Elliott, F., Falck, E., et al. (2021). SS-MSC2 Process cruise/mooring service 2020: Cruise Report, *The Nansen Legacy Report Series* (Vol. *20*). https://doi.org/10.7557/nlrs.5798

Firing, E., & Ranada, J. (1995). *Processing ADCP data with the CODAS software system version 3.1*. Joint Institute for Marine and Atmospheric Research, University of Hawaii and National Oceanographic Data Center.

Frajka-Williams, E., Eriksen, C. C., Rhines, P. B., & Harcourt, R. R. (2011). Determining vertical water velocities from Seaglider. *Journal of Atmospheric and Oceanic Technology*, *28*(12), 1641–1656. https://doi.org/10.1175/2011jtecho830.1

Garau, B., Ruiz, S., Zhang, W. G., Pascual, A., Heslop, E., Kerfoot, J., & Tintoré, J. (2011). Thermal lag correction on Slocum CTD glider data. *Journal of Atmospheric and Oceanic Technology*, *28*(9), 1065–1071. https://doi.org/10.1175/jtech-d-10-05030.1

Gawarkiewicz, G., & Plueddemann, A. J. (1995). Topographic control of thermohaline frontal structure in the Barents Sea Polar Front on the south flank of Spitsbergen Bank. *Journal of Geophysical Research*, *100*(C3), 4509–4524. https://doi.org/10.1029/94JC02427

Gerland, S., Ingvaldsen, R. B., Reigstad, M., Sundfjord, A., Bogstad, B., Chierici, M., et al. (2023). Still Arctic?The changing Barents Sea. *Elementa: Science of the Anthropocene*, *11*(1), 00088. https://doi.org/10.1525/elementa.2022.00088

Hamre, J. (1994). Biodiversity and exploitation of the main fish stocks in the Norwegian - Barents Sea ecosystem. *Biodiversity & Conservation*, *3*(6), 473–492. https://doi.org/10.1007/BF00115154

Helland-Hansen, B., & Nansen, F. (1909). The Norwegian Sea - Its physical oceanography based upon the Norwegian researches 1900–1904. *Report on Norwegian Fishery and Marine Investigations*, *11*(2), 360.

Holliday, N. P., Bersch, M., Berx, B., Chafik, L., Cunningham, S., Florindo-López, C., et al. (2020). Ocean circulation causes the largest freshening event for 120 years in eastern subpolar North Atlantic. *Nature Communications*, *11*(1), 585. https://doi.org/10.1038/s41467-020-14474-y

Ingvaldsen, R., Loeng, H., & Asplin, L. (2002). Variability in the Atlantic inflow to the Barents Sea based on a one-year time series from moored current meters. *Continental Shelf Research*, *22*(3), 505–519. https://doi.org/10.1016/S0278-4343(01)00070-X

Ingvaldsen, R. B. (2005). Width of the North Cape Current and location of the Polar Front in the western Barents Sea. *Geophysical Research Letters*, *32*(16), L16603. https://doi.org/10.1029/2005GL023440

Ingvaldsen, R. B., Assmann, K. M., Primicerio, R., Fossheim, M., Polyakov, I. V., & Dolgov, A. V. (2021). Physical manifestations and ecological implications of Arctic Atlantification. *Nature Reviews Earth & Environment*, *2*(12), 874–889. https://doi.org/10.1038/s43017-021-00228-x

IOC, SCOR, & IAPSO. (2010). *The international thermodynamic equation of seawater – 2010: Calculations and use of thermodynamic properties*, *Intergovernmental Oceanographic Commission, Manuals and Guides* (56th ed.). UNESCO.

Jakobsson, M., Mayer, L. A., Bringensparr, C., Castro, C. F., Mohammad, R., Johnson, P., et al. (2020). The international bathymetric chart of the Arctic Ocean version 4.0. *Scientific Data*, *7*(1), 176. https://doi.org/10.1038/s41597-020-0520-9

Johannesen, E., Ingvaldsen, R. B., Bogstad, B., Dalpadado, P., Eriksen, E., Gjøsæter, H., et al. (2012). Changes in Barents Sea ecosystem state, 1970–2009: Climate fluctuations, human impact, and trophic interactions. *ICES Journal of Marine Science*, *69*(5), 880–889. https://doi.org/10.1093/icesjms/fss046

Johannessen, O. M., & Foster, L. A. (1978). A note on the topographically controlled Oceanic Polar Front in the Barents Sea. *Journal of Geophysical Research*, *83*(C9), 4567–4571. https://doi.org/10.1029/JC083iC09p04567

Kolås, E. H., Fer, I., & Baumann, T. M. (2024). The Polar Front in the northwestern Barents Sea: Structure, variability and mixing. *Ocean Science*, *20*, 895–916. https://doi.org/10.5194/os-20-895-2024

Kolås, E. H., Fer, I., Peterson, A., Brakstad, A., & Elliot, F. (2022). Physical oceanography data from gliders in the Barents Sea, August 2019–February 2021 [Dataset]. *Norwegian Marine Data Centre*. https://doi.org/10.21335/NMDC-381060465

Kolås, E. H., Koenig, Z., Fer, I., Nilsen, F., & Marnela, M. (2020). Structure and transport of Atlantic Water north of Svalbard from observations in summer and fall 2018. *Journal of Geophysical Research: Oceans*, *125*(9), e2020JC016174. https://doi.org/10.1029/2020JC016174

Li, S., & McClimans, T. A. (1998). The effects of winds over a barotropic retrograde slope current. *Continental Shelf Research*, *18*(5), 457–485. https://doi.org/10.1016/S0278-4343(97)00077-0

Lien, V. S., Schlichtholz, P., Skagseth, Ø., & Vikebø, F. B. (2017). Wind-driven Atlantic water flow as a direct mode for reduced Barents Sea ice cover. *Journal of Climate*, *30*(2), 803–812. https://doi.org/10.1175/JCLI-D-16-0025.1

Lind, S., & Ingvaldsen, R. B. (2012). Variability and impacts of Atlantic water entering the Barents Sea from the north. *Deep Sea Research Part I: Oceanographic Research Papers*, *62*, 70–88. https://doi.org/10.1016/j.dsr.2011.12.007

Lind, S., Ingvaldsen, R. B., & Furevik, T. (2018). Arctic warming hotspot in the northern Barents Sea linked to declining sea-ice import. *Nature Climate Change*, *8*(7), 634–639. https://doi.org/10.1038/s41558-018-0205-y

Loeng, H. (1991). Features of the physical oceanographic conditions of the Barents Sea. *Polar Research*, *10*(1), 5–18. https://doi.org/10.3402/polar.v10i1.6723

Loeng, H., Ozhigin, V., & Ådlandsvik, B. (1997). Water fluxes through the Barents Sea. *ICES Journal of Marine Science*, *54*(3), 310–317. https://doi.org/10.1006/jmsc.1996.0165

McDougall, T. J., & Barker, P. M. (2011). *Getting started with TEOS-10 and the Gibbs Seawater (GSW) Oceanographic Toolbox* (p. 28). SCOR/IAPSO WG127.

Mohamed, B., Nilsen, F., & Skogseth, R. (2022). Interannual and decadal variability of sea surface temperature and sea ice concentration in the Barents Sea. *Remote Sensing*, *14*(17), 4413. https://doi.org/10.3390/rs14174413

Nilsen, F., Fer, I., Baumann, T. M., Breivik, Ø., Czyz, C., Frank, L., et al. (2021). PC-2 Winter Process Cruise (WPC): Cruise Report, *The Nansen Legacy Report Series* (Vol. *26*). https://doi.org/10.7557/nlrs.6324

Onarheim, I. H., & Årthun, M. (2017). Toward an ice-free Barents Sea. *Geophysical Research Letters*, *44*(16), 8387–8395. https://doi.org/10.1002/2017GL074304

Onarheim, I. H., Smedsrud, L. H., Ingvaldsen, R. B., & Nilsen, F. (2014). Loss of sea ice during winter north of Svalbard. *Tellus A: Dynamic Meteorology and Oceanography*, *66*(1), 23933–23941. https://doi.org/10.3402/tellusa.v66.23933

Orvik, K. A. (2022). Long-term moored current and temperature measurements of the Atlantic inflow into the Nordic Seas in the Norwegian Atlantic Current; 1995–2020. *Geophysical Research Letters*, *49*(3), e2021GL096427. https://doi.org/10.1029/2021GL096427

Orvik, K. A., & Niiler, P. (2002). Major pathways of Atlantic water in the northern North Atlantic and Nordic Seas toward Arctic. *Geophysical Research Letters*, *29*(19). 2-1–2-4. https://doi.org/10.1029/2002GL015002

Oziel, L., Sirven, J., & Gascard, J.-C. (2016). The Barents Sea frontal zones and water masses variability (1980–2011). *Ocean Science*, *12*(1), 169–184. https://doi.org/10.5194/os-12-169-2016

Padman, L., & Erofeeva, S. (2004). A barotropic inverse tidal model for the Arctic Ocean. *Geophysical Research Letters*, *31*(2), L02303. https://doi.org/10.1029/2003gl019003

Parsons, A. R., Bourke, R. H., Muench, R. D., Chiu, C.-S., Lynch, J. F., Miller, J. H., et al. (1996). The Barents Sea Polar Front in summer. *Journal of Geophysical Research*, *101*(C6), 14201–14221. https://doi.org/10.1029/96JC00119

Poulain, P.-M., Warn-Varnas, A., & Niiler, P. P. (1996). Near-surface circulation of the Nordic Seas as measured by Lagrangian drifters. *Journal of Geophysical Research*, *101*(C8), 18237–18258. https://doi.org/10.1029/96JC00506

Reigstad, M., Wassmann, P., Wexels Riser, C., Øygarden, S., & Rey, F. (2002). Variations in hydrography, nutrients and chlorophyll a in the marginal ice-zone and the central Barents Sea. *Journal of Marine Systems*, *38*(1), 9–29. https://doi.org/10.1016/S0924-7963(02)00167-7

Rudels, B., Björk, G., Nilsson, J., Winsor, P., Lake, I., & Nohr, C. (2005). The interaction between waters from the Arctic Ocean and the Nordic Seas north of Fram Strait and along the East Greenland Current: Results from the Arctic Ocean-02 Oden expedition. *Journal of Marine Systems*, *55*(1–2), 1–30. https://doi.org/10.1016/j.jmarsys.2004.06.008

Schauer, U., Loeng, H., Rudels, B., Ozhigin, V. K., & Dieck, W. (2002). Atlantic water flow through the Barents and Kara Seas. *Deep Sea Research Part I: Oceanographic Research Papers*, *49*(12), 2281–2298. https://doi.org/10.1016/S0967-0637(02)00125-5

Seaglider Quality Control Manual. (2012). *Seaglider Quality Control Manual (Version 1.11 ed.)*. School of Oceanography and Applied Physics Laboratory University of Washington.

Skagseth, Ø. (2008). Recirculation of Atlantic water in the western Barents Sea. *Geophysical Research Letters*, *35*(11), L11606. https://doi.org/10.1029/2008GL033785

Skagseth, Ø., Eldevik, T., Årthun, M., Asbjørnsen, H., Lien, V. S., & Smedsrud, L. H. (2020). Reduced efficiency of the Barents Sea cooling machine. *Nature Climate Change*, *10*(7), 661–666. https://doi.org/10.1038/s41558-020-0772-6

Skagseth, Ø., Furevik, T., Ingvaldsen, R., Loeng, H., Mork, K. A., Orvik, K. A., & Ozhigin, V. (2008). Volume and heat transports to the Arctic Ocean via the Norwegian and Barents Seas. In R. R. Dickson, J. Meincke, & P. Rhines (Eds.), *Arctic–Subarctic Ocean Fluxes: Defining the Role of the Northern Seas in Climate* (pp. 45–64). Springer Netherlands. https://doi.org/10.1007/978-1-4020-6774-7_3

Skogseth, R., Ellingsen, P., Berge, J., Cottier, F., Falk-Petersen, S., Ivanov, B., et al. (2019). UNIS hydrographic database [Dataset]. *Norwegian Polar Institute*. https://doi.org/10.21334/unis-hydrography

Smedsrud, L. H., Esau, I., Ingvaldsen, R. B., Eldevik, T., Haugan, P. M., Li, C., et al. (2013). The role of the Barents Sea in the Arctic climate system. *Reviews of Geophysics*, *51*(3), 415–449. https://doi.org/10.1002/rog.20017

Smedsrud, L. H., Ingvaldsen, R., Nilsen, J. E. Ø., & Skagseth, Ø. (2010). Heat in the Barents Sea: Transport, storage, and surface fluxes. *Ocean Science*, *6*(1), 219–234. https://doi.org/10.5194/os-6-219-2010

Smedsrud, L. H., Muilwijk, M., Brakstad, A., Madonna, E., Lauvset, S. K., Spensberger, C., et al. (2022). Nordic Seas heat loss, Atlantic inflow, and Arctic sea ice cover over the last century. *Reviews of Geophysics*, *60*(1), e2020RG000725. https://doi.org/10.1029/2020RG000725

Sundfjord, A., Assmann, K. M., Lundesgaard, Ø., Renner, A. H. H., Lind, S., & Ingvaldsen, R. B. (2020). Suggested water mass definitions for the central and northern Barents Sea, and the adjacent Nansen Basin: Workshop Report, *The Nansen Legacy Report Series* (Vol. *8*). https://doi.org/10.7557/nlrs.5707

Timmermans, M.-L., & Marshall, J. (2020). Understanding Arctic Ocean circulation: A review of ocean dynamics in a changing climate. *Journal of Geophysical Research: Oceans*, *125*(4), e2018JC014378. https://doi.org/10.1029/2018JC014378

Troupin, C., Beltran, J. P., Heslop, E., Torner, M., Garau, B., Allen, J., et al. (2015). A toolbox for glider data processing and management. *Methods in Oceanography*, *13–14*, 13–23. https://doi.org/10.1016/j.mio.2016.01.001

Våge, S., Basedow, S. L., Tande, K. S., & Zhou, M. (2014). Physical structure of the Barents Sea Polar Front near Storbanken in August 2007. *Journal of Marine Systems*, *130*, 256–262. https://doi.org/10.1016/j.jmarsys.2011.11.019

Visbeck, M. (2002). Deep velocity profiling using lowered acoustic Doppler current profilers: Bottom track and inverse solutions. *Journal of Atmospheric and Oceanic Technology*, *19*(5), 794–807. https://doi.org/10.1175/1520-0426(2002)019⟨0794:dvpula⟩2.0.co;2